Template-stripped Plasmonic Cup Resonators for Single-Nanohole-Based Sensing and Spectroscopy

A Thesis

SUBMITTED TO THE FACULTY OF THE
UNIVERSITY OF MINNESOTA BY

Stephen Andrew Olaf Olson

IN PARTIAL FULFILLMENT OF THE
REQUIREMENTS FOR THE DEGREE OF

MASTER OF SCIENCE IN
ELECTRICAL ENGINEERING

Adviser: Sang-Hyun Oh

May 2015

Acknowledgements

I would like to thank my advisor, Professor Sang-Hyun Oh, for his guidance and support over the course of this research, as well as our collaborator, Dr. Henri Lezec, for his contributions to this project. I also thank Professor James Leger and Professor Taner Akkin for serving on my thesis committee.

Scientific research is always a team effort, consequently the work represented in this thesis would not have been possible without the assistance and advice of my colleagues. I would like to recognize Dr. Jonah Shaver, Dan Mohr, Dr. Timothy Johnson, Luke Jordan, Dan Klemme, and Dr. Yong-Sang Ryu for their direct contributions to this research. I would also like to express my gratitude to other members of our research group , Avijit Barak, Shailabh Kumar, Daehan Yoo, Xiaoshu Chen, Lauren Otto, Dr. Nate Wittenburg, Dr. Hyeong-Ryeol Park, Dr. Seon Namgung, Dr. Jincy Jose, and Dr. Sudhir Cherukulappurath, for their comradery, feedback, and moral support.

Template-stripped Plasmonic Cup Resonators for Single-Nanohole-Based Sensing and Spectroscopy

by Stephen Andrew Olaf Olson

ABSTRACT

We have designed and tested a new plasmonic biosensor, featuring a centered nanohole in the base of a recessed metallic nanocup. This configuration enables us to perform independent plasmon-resonance-enhanced single-nanohole transmission spectroscopy on femtoliter volumes of solution. In this thesis we will demonstrate the fabrication, characterization, and application of these novel cup resonator plasmonic biosensors. Utilizing plasmonic confinement to enhance and modulate transmission through a nanohole aperture, the resulting transmission spectra can be used to determine changes in the material properties of a dielectric material located inside the sensing volume of the cup. We have determined, through measurements and simulations, the physical mechanisms causing transmission modulation through the structure. Utilizing this information, we have constructed predictive behavior models for the design and customization of these devices for specific purposes. We show that these structures are responsive to refractive index changes in their surroundings, and propose some possible application of these resonators in biological sensing roles which take advantage of their unique geometry.

Contents

List of Figures

1 Theory

The devices discussed in this thesis operate using confined surface plasmon polariton (SPP) resonances to modulate transmission through a subwavelength nanohole. The underlying physical principles behind SPPs can be derived using selected topics from macroscopic electromagnetic theory. In this section, we will attempt to establish a basic understanding of the physics behind surface plasmons in order to better explain the behavior of our device [1, 2, 3, 4].

1.1 Maxwell's Equations

Maxwell's equations for macroscopic electromagnetism describe the relationship between the four electromagnetic fields: $\mathbf{D}$, the dielectric displacement (units C/m^2); $\mathbf{E}$, the electric field (V/m); $\mathbf{H}$, the magnetic field (A/m); and $\mathbf{B}$, the magnetic induction/magnetic flux density (N/(A$\cdot$ m). The four equations listed below are known individually as Gauss's Law (Flux Theorem), Gauss's Law for Magnetism, Faraday's Law of Induction, and Ampere's Law (with Maxwell's addition).This grouping of equations provides the fundamental foundation for all modern electromagetic theory.

$$\nabla \cdot \mathbf{D} = \rho_{\mathbf{f}} \tag{1.1.1}$$

$$\nabla \cdot \mathbf{B} = \mathbf{0} \tag{1.1.2}$$

$$\nabla \times \mathbf{E} = -\frac{\partial \mathbf{B}}{\partial t} \tag{1.1.3}$$

$$\nabla \times \mathbf{H} = \mathbf{J_f} + \frac{\partial \mathbf{D}}{\partial t} \tag{1.1.4}$$

Because of the macroscopic nature of our analysis, we have made the distinction between free and bound charge and current. Free charge in the system dictated by $\rho_{\mathbf{f}}$, and free current is written as $\mathbf{J_f}$. Free charge and current are considered external stimuli to the system, whereas bound charge and current are the inherent material responses to external stimuli. These bound charges and currents can be expressed in the polarization and magnetization of a material, respectively. Polarization and magnetization are defined by the following constitutive relations.

The relationship between the dielectric displacement, the electric field, and the material polarization is determined by:

$$\mathbf{D} = \epsilon_{\mathbf{0}}\epsilon\mathbf{E} + \mathbf{P} \tag{1.1.5}$$

where the polarization, $\mathbf{P}$, is the is the electric dipole moment per unit volume inside of the material, ϵ_0 is the permittivity of free space ($\sim 8.854 \times 10^{-12}$ F/m), and ϵ is the dielectric permittivity of the material.

The magnetic field and magnetic induction are linked through magnetization via

$$\mathbf{H} = \frac{\mathbf{1}}{\mu_\mathbf{0}\mu}\mathbf{B} - \mathbf{M} \tag{1.1.6}$$

where the magnetization, $\mathbf{M}$, describes the density of magnetic dipole moments in the material, μ_0 is the magnetic permeability in vacuum ($\sim 1.257 \times 10^{-6}$ H/m), and μ is the magnetic permeability of the material (for non-magenetic materials $\mu = 1$).

Because the primary metal discussed in this thesis will be silver, which is not ferromagnetic, for the purposes of analyis, we will make the assumption that $\mathbf{M} = \mathbf{0}$ henceforth.

1.2 Wave Equation in Vacuum

In regions of space absent of charge and current, we can easily manipulate Maxwell's equations to reveal the relationship of an electric or magnetic field within space and time. In such an environment, there is no material polarization, and so $\mathbf{D} = \epsilon_\mathbf{0}\epsilon\mathbf{E}$. Additionally, because of the absence of charge, $\nabla \cdot \mathbf{D} = \mathbf{0}$, and so now consequently, $\nabla \cdot \mathbf{E} = \mathbf{0}$. Further more, because of the absence of current, $\mathbf{J_f} = \mathbf{0}$.

The following derivation will be performed for the case of an electric field. The derivation for a magnetic field follows a similar approach and is left as an exercise for the reader. We begin by applying a curl to both sides of equation 1.1.3

$$\nabla \times (\nabla \times \mathbf{E}) = \nabla \times (-\frac{\partial \mathbf{B}}{\partial t}) \tag{1.2.1}$$

This equation, combined with the following identity

$$\nabla \times (k\mathbf{A}) = k(\nabla \times \mathbf{A}) \tag{1.2.2}$$

leads to

$$\nabla \times (\nabla \times \mathbf{E}) = -\frac{\partial}{\partial t}(\nabla \times \mathbf{B}) \tag{1.2.3}$$

into which we may substitute equation 1.1.4, enabling us to decouple the electric field from the magnetic field, leading to the following expression:

$$\nabla \times (\nabla \times \mathbf{E}) = -\mu_\mathbf{0}\frac{\partial^\mathbf{2}\mathbf{D}}{\partial t^\mathbf{2}} \tag{1.2.4}$$

Now, using another identity from vector calculus

$$\nabla \times (\nabla \times \mathbf{E}) \equiv \nabla(\nabla \cdot \mathbf{E}) - \nabla^\mathbf{2}\mathbf{E} \tag{1.2.5}$$

and remembering that, in our system, $\mathbf{D} = \epsilon_\mathbf{0}\epsilon\mathbf{E}$ and $\nabla \cdot \mathbf{E} = \mathbf{0}$, enables us to further simplify equation 1.2.1 to the following form, known as the wave equation:

$$\nabla^2\mathbf{E} - \frac{\epsilon}{c^2}\frac{\partial^\mathbf{2}\mathbf{E}}{\partial t^\mathbf{2}} = \mathbf{0} \tag{1.2.6}$$

Here $c = \frac{1}{\sqrt{\epsilon_0\mu_0}}$ is the speed of the traveling wave (in vacuum, $\epsilon = 1$). This value may be more famously known as the speed of light in vacuum ($\sim$ 299,792,458 m/s). However, when it was first calculated by Maxwell in 1862, such a value came as a bit of a surprise. Though the wave equation itself was not a new discovery (it had first been solved nearly 100 years prior by Euler and d'Alembert) [5] , the speed at which the wave was propagating was astounding to Maxwell. Previously, experiments had measured the speed at which light traveled here on earth, and Maxwell's calculated velocity of propagating electromagnetic waves in vacuum closely matched those numbers. He famously remarked, "We can scarcely avoid the inference that light consists in the transverse undulation of the same medium which is the cause of electric and magnetic phenomenon" [6]. As we know today, Maxwell was correct in his inference: light is a propagating electromagnetic wave.

Continuing on, we can manipulate this remarkable expression into a more useful form. If we assume a harmonic time dependence of the electric field such that $\mathbf{E}(\mathbf{r}, t) = \mathbf{E}(\mathbf{r})\mathbf{e}^{-i\omega t}$, and insert this relation into equation 1.2.6, we arrive at the Helmholtz equation for propagating waves:

$$\nabla^2\mathbf{E} + {k_0}^2\epsilon\,\mathbf{E} = \mathbf{0} \tag{1.2.7}$$

Here ${k_0}^2 = \left(\frac{\omega}{c}\right)^2 = k_x^2 + k_y^2 + k_z^2$ is known as the wavevector of the propagating wave in a vacuum. It can also be written as the magnitude of all directional wavevectors. This form of the wave equation is used frequently in optics, and we will use it in our discussion of surface plasmon polaritions.

1.3 Dielectric Function of a Metal

To determine the dielectric function of a conductor, we can use a plasma model to approximate the behavior of electrons in the material. This approach is known as the free electron gas model. It imagines clouds of free electrons moving collectively against a fixed background of positively charged atomic nuclei in response to an external stimulus. This gas of free electrons gives metals their conductive properties. A simple model, it does not account for more intricate effects such as electron-electron interaction or lattice potential. Nevertheless, this model will provide sufficient insight into the response of conductive materials for our purposes.

Because of their free gas-like nature, electrons in a conductor are free to move in response to stimulating electromagnetic fields. As discussed in section 1.2, light is a propagating electromagnetic wave. When exposed to light, electrons respond following the Lorentz force law. This results in a collective oscillation of electrons in the material. However because this is a real material, the electron motion is damped by collisions. These collisions occur with a characteristic frequency, $\gamma = \frac{1}{\tau}$, where τ is the relaxation time of the free electron gas (10^{-14} seconds at 300 K), giving a collision frequency of 100 THz. Furthermore, because they are not simply charges in a vacuum, we must account for electron behavior by assuming they posses an effective mass, m; this is the mass the particle seems to have when responding to forces. In this case, because the forces are optical, the value of the effective mass is a function of the impinging photon frequency and the temperature of the material [7]. Armed with the idea that electrons oscillate with the applied electric field, while also experiencing damping, we can model their behavior as a damped harmonic oscillator:

$$m\ddot{\mathbf{x}} + m\gamma\dot{\mathbf{x}} = -e\mathbf{E} \tag{1.3.1}$$

Again assuming a time dependence of the driving electric field, $\mathbf{E}(\mathbf{r}, t) = \mathbf{E}(\mathbf{r})\mathbf{e}^{-i\omega t}$, a solution for the position of electrons in the electric field from equation 1.3.1 is described by $\mathbf{x}(t) = \mathbf{x_0}(t)e^{-i\omega t}$. Plutting this solution into the harmonic oscillator equation reveals the following relationship:

$$\mathbf{x}(t) = \frac{e\mathbf{E}(t)}{m(\omega^2 + i\gamma\omega)} \tag{1.3.2}$$

From electrostatics we recall that polarization is defined as the average dipole moment per unit volume:

$$\mathbf{P} = \frac{\langle \mathbf{p} \rangle}{V} \tag{1.3.3}$$

where the dipole moment is defined as charge multiplied by the displacement vector between negative and positive charges

$$\mathbf{p} = q\mathbf{d} \tag{1.3.4}$$

Given the number density of electrons, n, and the charge of an electron, e, we can equate

$$\frac{q}{V} = ne \tag{1.3.5}$$

As the collective group of electrons (region of negative charge) moves away from its initial position $\mathbf{x_0}$, the vacated region will then become a localized region of positive charge. Due to the statistical distribution of the electrons moving in response to the electric field, we can say that the displacement

vector is equal to the average position of the electrons, represented by $\mathbf{x(t)}$. thus equating $\mathbf{x}(t)$ to $\langle \mathbf{d} \rangle$. Therefore,

$$\mathbf{P} = ne\mathbf{x}(t) \tag{1.3.6}$$

and consequently

$$\mathbf{P} = \frac{ne^2\mathbf{E}(t)}{m(\omega^2 + i\gamma\omega)} \tag{1.3.7}$$

Furthermore, recalling that $\mathbf{D} = \epsilon_\mathbf{0}\mathbf{E} + \mathbf{P}$ for real materials, gives us

$$\mathbf{D} = \epsilon_\mathbf{0}\left(\mathbf{1} - \frac{\omega_p^\mathbf{2}}{(\omega^\mathbf{2} + i\gamma\omega)}\right)\mathbf{E} \tag{1.3.8}$$

where ω_p is defined as

$$\omega_p = \sqrt{\frac{ne^2}{m\epsilon_0}} \tag{1.3.9}$$

ω_p is known as the plasma frequency of the free electron gas. This frequency describes the transition frequency between metallic and dielectric behavior in the metal. For silver, it is $2.18\times10^{15}\mathrm{s}^{-1}$ [8]. Using this relation, the relative permittivity of the metal can be expressed

$$\begin{aligned}\epsilon(\omega) &= 1 - \frac{\omega_p^2}{(\omega^2 + i\gamma\omega)} \\ &= \epsilon_1(\omega) + i\,\epsilon_2(\omega)\end{aligned} \tag{1.3.10}$$

Equation 1.3.10 is known as the 'Drude' model. The real, ϵ_1, and imaginary, ϵ_2, components are extracted (using $\tau = \frac{1}{\gamma}$)

$$\epsilon_1(\omega) = 1 - \frac{\omega_p^2\,\tau^2}{1 + \omega^2\tau^2} \tag{1.3.11}$$

$$\epsilon_2(\omega) = \frac{\omega_p^2\,\tau^2}{\omega\,(1 + \omega^2\tau^2)} \tag{1.3.12}$$

These equations are relevant because one of the characteristics of a metal is that the real component of its relative permittivity must be negative. This property is what prevents electromagnetic waves from penetrating the metal, giving metals their characteristic reflective shine. Based on the equations shown above, this means that the oscillation frequency of the free electron cloud must be lower than the plasma frequency ($\omega < \omega_P$) for a metal to retain its metallic character. For frequencies near the plasma frequency limit, the imaginary component becomes negligble, and we can estimate the dielectric function (1.3.10) using

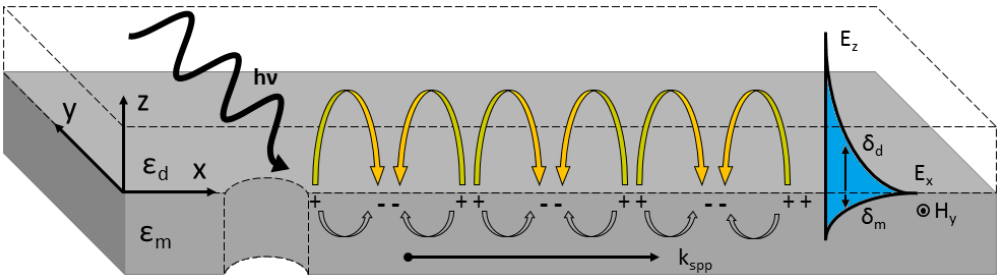

Figure 1: Surface plasmon polariton generation. The system consists of a dielectric layer (permittivity ϵ_d) and a metal layer (permittivity ϵ_m). There is a nanohole milled through the metal layer. This surface 'defect' provides additional momentum to scattered photons (initial energy $h\nu$), enabling them to couple into plasmon modes on the surface of the metal. These plasmon waves propagate with a wavevector (k_{spp}) until they decay. Penetration depth into the metal and dielectric is given by δ_d and δ_m respectively.

$$\epsilon(\omega) \approx 1 - \frac{\omega_p^2}{\omega^2} \tag{1.3.13}$$

This expressionwill be useful in our discussion of surface plasmon polaritons (SPPs) at a metal-dielectric interface.

1.4 Surface Plasmon Polaritons

The simplest system able to support surface plasmon polaritons is a metal-dielectric interface, with an interfacial boundary that lies in the x-y plane (Figure 1). For additional simplicity we can assume that the electromagnetic wave propagates along the x-axis with no variation in the y-direction. Because we are interested in finding a wave solution at the interface of these two materials, it is helpful to think of the relative permittivity as function of both frequency and vertical position, $\epsilon(\omega, z)$. If the direction of propagation is purely in the x-direction, and the electric field has harmonic time dependence, field will only spatially dependent in one dimension: $\mathbf{E}(x, y, z) = \mathbf{E}(z)e^{i(k_x x - \omega t)}$. If this simplified electric field expression is input into the Helmholtz equation we find:

$$\nabla^2 \mathbf{E}(z)e^{ik_x x} + k_0^2\, \epsilon\, \mathbf{E}(z)e^{ik_x x} = 0 \tag{1.4.1}$$

which equals

$$\frac{\partial^2 \mathbf{E}(z)}{\partial z^2} e^{ik_x x} + \frac{\partial^2 e^{ik_x z}}{\partial z^2} \mathbf{E}(z) + k_0^2\, \epsilon\, \mathbf{E}(z)e^{ik_x x} = 0 \tag{1.4.2}$$

simplified

$$\frac{\partial^2 \mathbf{E}(z)}{\partial z^2} + (k_0^2 \epsilon - k_x^2)\, \mathbf{E}(z) = 0 \tag{1.4.3}$$

This equation is commonly found in other photonics applications such as waveguides [9]. Due to the orthogonal relationship between **B** and **E**, a similar equation can be derived for the magnetic field.

In order to determine the spatial field profile and the dispersion of the propagating wave, we should derive explicit expressions for each field component of E and H. These relationships can be simply determined by expanding Faradays law of induction and Amperes current law into their Cartesian components while continuing to assume the harmonic time dependence of the field ($\frac{\partial}{\partial t} = i\,\omega$).

Faraday's Law:

$$\frac{\partial E_z}{\partial y} - \frac{\partial E_y}{\partial z} = i\omega\mu_0 H_x \tag{1.4.4}$$

$$\frac{\partial E_x}{\partial z} - \frac{\partial E_z}{\partial x} = i\omega\mu_0 H_y \tag{1.4.5}$$

$$\frac{\partial E_y}{\partial x} - \frac{\partial E_x}{\partial y} = i\omega\mu_0 H_z \tag{1.4.6}$$

Ampere's Law:

$$\frac{\partial H_z}{\partial y} - \frac{\partial H_y}{\partial z} = -i\omega\epsilon_0\epsilon E_x \tag{1.4.7}$$

$$\frac{\partial H_x}{\partial z} - \frac{\partial H_z}{\partial x} = -i\omega\epsilon_0\epsilon E_y \tag{1.4.8}$$

$$\frac{\partial H_y}{\partial x} - \frac{\partial H_x}{\partial y} = -i\omega\epsilon_0\epsilon E_z \tag{1.4.9}$$

Because of the simplified geometry of our situation, where we assume the electromagnetic wave is only propagating in the x-direction, we can assume that $\frac{\partial}{\partial x} = ik_x$ and $\frac{\partial}{\partial y} = 0$. Based on these assumptions, equations 1.4.4 - 1.4.9 can be simplified

$$\frac{\partial E_y}{\partial z} = -i\omega\mu_0 H_x \tag{1.4.10}$$

$$\frac{\partial E_x}{\partial z} - ik_x E_z = i\omega\mu_0 H_y \tag{1.4.11}$$

$$ik_x E_y = i\omega\mu_0 H_z \tag{1.4.12}$$

$$\frac{\partial H_y}{\partial z} = i\omega\epsilon_0\epsilon E_x \tag{1.4.13}$$

$$\frac{\partial H_x}{\partial z} - ik_x H_z = -i\omega\epsilon_0\epsilon E_y \tag{1.4.14}$$

$$ik_x H_y = -i\omega\epsilon_0\epsilon E_z \tag{1.4.15}$$

Upon inspection, it is revealed that these simplified equations can be grouped into two independent sets. These sets describe the polarization of the electromagnetic wave in reference to the metal-dielectric interface. The two groupings are referred to as Transverse Magnetic (TM) and Transverse Electric (TE) polarized waves. TM polarization occurs when the the magnetic field is transverse to the surface interface plane. Rearranging equations 1.4.13, 1.4.15

$$E_x = -i\frac{1}{\omega\epsilon_0\epsilon}\frac{\partial H_y}{\partial z} \tag{1.4.16}$$

$$E_z = -\frac{k_x}{\omega\epsilon_0\epsilon}H_y \tag{1.4.17}$$

and combining them with equation 1.4.11 reveals the wave equation for TM modes:

$$\frac{\partial^2 H_y}{\partial z^2} + \left(k_0^2\epsilon - k_x^2\right) H_y = 0 \tag{1.4.18}$$

An identical procedure can be performed to find the wave equation for TE polarized waves. In this case, it is the electric field which is transverse to the material interface. Rearranging equations 1.4.10 and 1.4.12

$$H_x = i\frac{1}{\omega\mu_0}\frac{\partial E_y}{\partial z} \tag{1.4.19}$$

$$H_z = \frac{k_x}{\omega\mu_0}E_y \tag{1.4.20}$$

and combining them with equation 1.14.14 reveals the wave equation for TE modes:

$$\frac{\partial^2 E_y}{\partial z^2} + \left(k_0^2\epsilon - k_x^2\right) E_y = 0 \tag{1.4.21}$$

Because an SPP is the coupling of a photon and the plasma oscillation of electrons in the metal, we must consider the dielectric constants of both materials: the real relative permittivity of the dielectric ϵ_d, and

the imaginary permittivity of the metal $\epsilon_m(\omega)$. Using the TM polarized wave equations derived above for each medium, we can solve the system using the continuity of H_y and $\epsilon\mathbf{E}$ at the material interface as boundary conditions.

The solution for equation 1.4.18 requires the form $H_y = Ae^{-kz}$, where A is an amplitude coefficient. By inspection this means that

$$k_{z,d}^2 = k_x^2 - k_0^2\epsilon_d \tag{1.4.22}$$

$$k_{z,m}^2 = k_x^2 - k_0^2\epsilon_m \tag{1.4.23}$$

The terms $k_{z,d}$ and $k_{z,m}$ inherently describe wavevectors in the z-direction, for positive and negative z respectively. Equations 1.4.22 and 1.4.23 offer critical insight into the nature of surface plasmon polaritons. These equations show that for the propagation constant of the surface plasmon, k_x, to be sufficiently large, k_z must be imaginary (in our system, k_y is zero). This means that the propagating wave must be evanescently decaying in the z-dimension. Therefore (including $e^{ik_x x}$ because the wave is propagating in the x-direction) we may write:

For $z > 0$ (in the dielectric)

$$H_y(z) = A_d e^{ik_x x} e^{-|k_{z,d}|z} \tag{1.4.24}$$

$$E_x(z) = iA_d \frac{1}{\omega\epsilon_0\epsilon_d} k_d e^{ik_x x} e^{-|k_{z,d}|z} \tag{1.4.25}$$

$$E_z(z) = -A_d \frac{k_x}{\omega\epsilon_0\epsilon_d} e^{ik_x x} e^{-|k_{z,d}|z} \tag{1.4.26}$$

For $z < 0$ (in the metal)

$$H_y(z) = A_m e^{ik_x x} e^{-|k_{z,m}|z} \tag{1.4.27}$$

$$E_x(z) = -iA_m \frac{1}{\omega\epsilon_0\epsilon_m} k_m e^{ik_x x} e^{|k_{z,m}|z} \tag{1.4.28}$$

$$E_z(z) = -A_m \frac{k_x}{\omega\epsilon_0\epsilon_m} e^{ik_x x} e^{|k_{z,m}|z} \tag{1.4.29}$$

Furthermore, continuity between the propagating TM waves in both the metal and the dielectric requires

$$\frac{k_{z,m}}{k_{z,d}} = -\frac{\epsilon_m}{\epsilon_d} \tag{1.4.30}$$

It is important to note that due to the sign convention applied here, continuity is only achievable if $\mathrm{Re}[\epsilon_m] < 0 < \epsilon_d$. This implies that surface waves are only sustainable at interfaces between materials with oppositely-signed real parts of permittivity, i.e. between a metal (conductor) and a dielectric (insulator). Solving for k_x between equations 1.4.22, 1.4.23, and 1.4.30 reveals the dispersion relation of a surface plasmon polariton propagating at the interface between a metal and a dielectric.

$$k_x = k_0 \sqrt{\frac{\epsilon_d \epsilon_m}{\epsilon_d + \epsilon_m}} = k_{spp} \tag{1.4.31}$$

We now have an expression for the k-vector of a surface plasmon, k_{spp}. It is important to note that this expression is valid for both real and complex values of ϵ_m. A similar analysis of these equations can be performed for TE modes, however, it merely reveals that continuity between confined surface waves is not possible for TE modes, and therefore the exercise is left to the reader. Because of this, surface plasmon polaritons can only exist for TM polarized light.

At this point it is logical to briefly touch on the generation of surface plasmons. Up to this point in our analysis we have discussed flat metal surfaces which seemingly respond plasmonically to incident light. However, in reality, this is not generally possible. As we mentioned when discussing equations 1.4.22 and 1.4.23, k_z must be imaginary in order for k_x to be large enough to fulfill $k_0^2 \epsilon = k_x^2 + k_z^2$. However, this increase in k_x does not come naturally, the system must be manipulated to enable a larger k-vector. This increase in momentum is generally achieved by one of two methods. One, known as a Kretschmann configuration involves placing a high index medium (e.g. a prism) on one side of a metallic thin film, and then coupling light from the high index side, through the film, onto the low index side. The coupled light retains its larger k_x momentum from propagating through the prism, enabling it to meet the necessary momentum conditions for surface plasmons on the open surface. The second method, which is the method used in the device presented in this thesis, utilizes 'defects' on the surface of the metal film to increase momentum. In this case, a 'defect' could be a groove, a corner-edge, a raised step, or a nanohole. When light impinges on one of these surface features, it is partially scattered. Some of the scattered photons, which posses the correct momentum and direction, are then able to couple into the metal surface, forming propagating surface plasmon waves. This process is illustrated in Figure 1. Therefore, equation 1.4.31 is critical to the understanding, design, and interpretation of plasmonic structures. It gives the specific momentum conditions necessary for the generation and sustainment of surface plasmon waves at a metal dielctric interface.

We can graphically illustrate the dispersion behavior of surface plas-

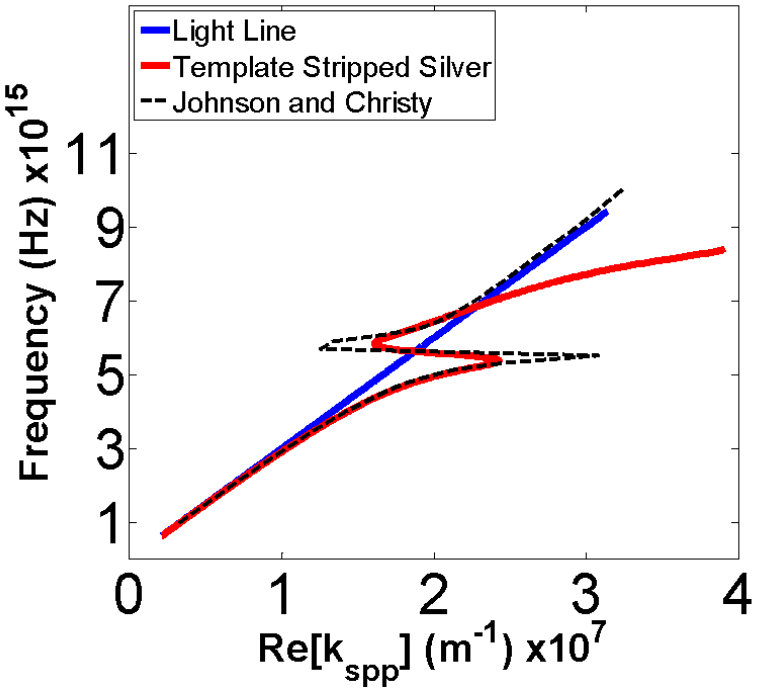

Figure 2: Dispersion curve for plasmons at a silver/air interface. Frequency is angular frequency (ω). A light line is plotted to illustrate the frequency/wavevector relationship of incident light. Included is a Lorentz-Drude fit, calculated from measured template stripped silver. This curve was used during FDTD simulations. We also plot values taken from Johnson and Christy [10]. We see that in in the visible regime (λ=400-900 nm, ω=4.7124 $\times$ 10^{15} to 2.0944 $\times$ 10^{15} s^{-1}), the measured fit aligns well with Johnson and Christy's data.

mons using the Drude approximation of equation 1.3.13, compared to the dispersion of light in other materials.

The slope of the dispersion curve is the group velocity of the wave, defined

$$\nu_g = \frac{\partial \omega}{\partial k} \tag{1.4.32}$$

As can be seen, the dispersion curves for surface plasmon waves lay to the right of the dispersion of light in other mediums. This demonstrates the additional momentum possessed by surface plasmon waves, excited using a technique that adds momentum, such as grating or prism coupling.

Addtionally, notice that as the wavevector increases, the frequency of the confined surface wave approaches a characteristic surface plasma frequency, ω_{sp}. This value can be calculated simply by inserting the Drude free-electron dielectric function (equation 1.3.13) into the surface plasmon

dispersion relation (Equation 1.4.31), and solving for frequency:

$$\omega_{sp} = \frac{\omega_p}{\sqrt{1+\epsilon_m}} \tag{1.4.33}$$

By using the Drude model, which assumes negligible damping, as the wavevector k_{spp} extends to infinity, the frequency becomes nearly constant, effectively causing the group velocity to go to zero. In this regime, the propagating wave acquires a nearly electrostatic character and is what we define as a *surface plasmon*.

Although our discussion of dispersion of surface plasmon polaritons to this point has used idealized permittivities to illustrate behavior, in reality, damping is not negligible and $\mathrm{Im}[\epsilon_m] \neq 0$. In physical systems, excited conduction band electrons are damped by other free electrons and interband effects. As alluded to in our discussion of k_{spp}, $\epsilon_d(\omega)$ and thus k_{spp} are usually complex. Because of these damping effects, the amplitude of the confined surface wave will eventually decay. Since the intensity of an electromagnetic wave goes by the square of the electric field

$$I \propto e^{2i(k_{spp,r}+ik_{spp,i})x} \tag{1.4.34}$$

the intensity will fall to $I \propto \frac{1}{e}$ when $x = \frac{1}{2k_{spp,i}}$. This characteristic length is called the propagation length of the surface plasmon and is often written

$$L = \frac{1}{2\,\mathrm{Im}[k_{spp}]} \tag{1.4.35}$$

While the values of $\mathrm{Im}[k_{spp}]$ are not explicitly clear from the analysis thus far, by plotting the propagation length vs incident wavelength (Figure 3), we see that L is minimized for short wavelengths, and maximizes as the incident wavelength increases. Additionally, as could be inferred from equations 1.4.24-26 the penetration depth of the field into the propagative medium is defined as

$$\delta_p \equiv \frac{1}{|k_{d,m}|} \tag{1.4.36}$$

where $k_{d,m}$ can also be expressed using equations 1.4.22/1.4.23 and 1.4.31

$$k_{d,m} = k_0\sqrt{\frac{-\epsilon_{d,m}^2}{\epsilon_d+\epsilon_m}} \tag{1.4.37}$$

As can be seen in Figure 3, the evanescent field penetrates between a quarter and full wavelength into the dielectric, whereas in metal it is constrained to the skin depth of the conductor. In conjunction with equation 1.4.35, this means that higher energy plasmon waves are more tightly confined to the surface, but also suffer from shorter propagation lengths, whereas lower

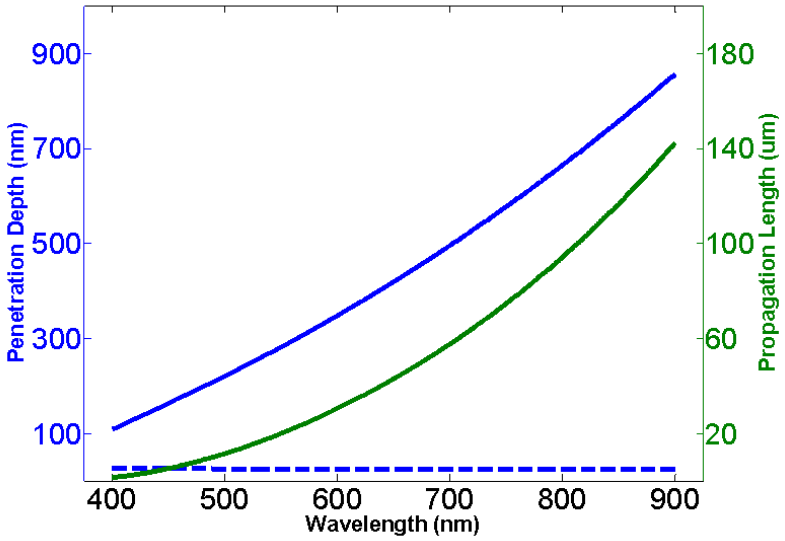

Figure 3: The penetration depth of surface plasmon waves is compared with their propagation length. This figure assumes an air/silver interface, and incorporates the Drude-Lorentz fit illustrated in Figure 2. The solid blue line is the penetration depth into air, whereas the dashed blue line is the penetration depth into silver ($\sim$ 25 nm). The green line is the propagation length of the surface wave. The wavelength is the incident light wavelength. This shows that longer wavelength surface plasmons are more weakly confined to the surface, but also propagate much farther distances.

energy waves can propagate much farther on the surface, but are weakly confined to the metal dielectric interface. These trends are illustrated in Figure 3. It is important to note that both types of waves possess properties that can be useful for different applications, such as surface and bulk refractive index sensing [11].

One of the common applications of plasmonic devices is to measure changes in the refractive index, n, of a material. As shown by equation 1.4.31, as the permittivity ($\epsilon_d = n^2$) of the dielectric changes, the value of k_{spp} also changes, because k_0 remains constant. For a given incident wavelength, the relative surface plasmon wavelength will shift as the refractive index of the material changes, resulting in measurable differences in SPP dispersion. However, as different plasmon wavelengths experience different degrees of surface confinement, they will be more or less sensitive to bulk or surface changes in the dielectric [12].

2 Device

Over the course of this research, we have developed a plasmonic cavity resonator capable of enhancing optical transmission through a single nanohole. This is achieved by placing a single nanohole aperture in the center of a recessed 'cup', hence the title 'cup resonator'. The vertical sidewalls of the cup function as mirrors to reflect propagating surface plasmon polaritons back to the source nanohole. These mirrors enable the buildup of plasmonic standing wave resonances inside the structure, which in turn modulate the transmission of light through the nanohole. This results in characteristic optical transmission spectra which are analyzed to determine device behavioral mechanisms. By changing material properties (such as refractive index) of the dielectric inside the structure, we can observe shifts in the transmission spectra. These shifts can be analyzed to determine the degree to which the dielectric material properties changed.

While our device is unique, there are aspects of the structure and mechanism that have also been demonstrated by other groups. Early experiments demonstrate that periodic grooves parallel to a narrow slit can enhance transmission when the slit is illuminated from the opposite side [13, 14, 15]. Later, others showed the possibility of using single grooves to excite propagating plasmons towards the illuminated slit, building interferometers which could be used to perform refractive index sensing experiments [16, 17, 18, 19]. In two-dimensional configurations, L-shaped [20, 21] and T-shaped [22, 23] trench-slit interferometers utilized sidewalls to reflect plasmons back on the transmission slit. In these experiments, transmission enhancement was observed by including higher refractive index dielectric layers in the trench. By incorporating radially-symmetric grooves around single nanohole apertures, it has been shown that plasmons can be focused onto the nanohole, enhancing and modulating transmission through the aperture; these sensors were used to perform reaction kinetics measurements [24]. The use of single nanoholes enables the construction of high-density, isolated sensor pixel arrays. However, these have never been combined with recessed cylindrical cavities in the silver film, although such structures have been studied elsewhere [25, 26, 27, 28] . Because of this, we have incorporated recessed metallic cylindrical cavities with single nanohole apertures and reflecting sidewalls to build a unique three dimensional plasmonic biosensor. By incorporating a microwell 'cup' into the sensor structure, unique application possibilities arise, which are unachievable by other means. These applications utilize the physically confining properties of the structures to trap and hold analytes in the sensor. This cannot be accomplished without the physical container that we have incorporated in our device.

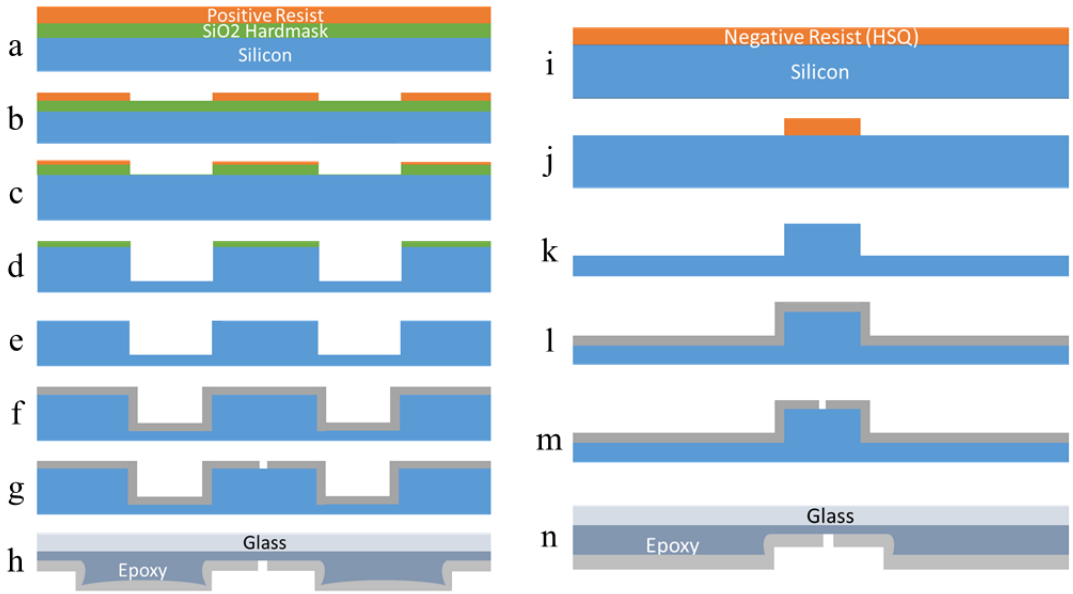

Figure 4: 2-D cross-sectional process flows showing cup resonator fabrication using both positive (a-h) and negative (i-n) electron beam resists. (a, i) Resist is spun on top of a thermally grown SiO_2 hardmask layer. (b, j) The resist is patterned using electron beam lithography. (c) Using the resist layer as an etch mask, the hardmask is removed by reactive ion etching. (d, k) The silicon is dry etched. (e) The SiO_2 hardmask is removed. (f, l) A silver thin film is sputtered on to the structure. (g, m) An aperture is milled through the silver film using a focused ion beam. (h, n) Optical epoxy is applied to the silver film to adhere it to a glass slide, and the patterned silver thin film is template stripped off the silicon mold. These final cross-sections are scaled to represent 200 nm apertures, 500 nm high sidewalls, and 2300 nm cup diameters. The width of the raised sidewalls in (h) is 3000 nm.

2.1 Fabrication

To fabricate these devices we chose to use electron beam lithography (EBL) to pattern the etch masks on the surface of the silicon wafer. Electron beam lithography was selected over traditional photolithography due to its higher resolution, and digitally controlled beam scanning resulting in easily customizable patterns. Similar to photolithography resists, there are two main categories for EBL resist: 'positive', wherein the exposed resist is removed during development, and 'negative', wherein the exposed resist remains on the wafer after development (unexposed resist is dissolved into the developer solvent). Originally, our devices were manufactured using a positive

EBL resist: Poly(methyl methacrylate) (PMMA). This method produces functioning cup resonators which utilize raised vertical sidewalls surrounding the nanohole to reflect and confine surface plasmon waves. However, in time, the fabrication process was updated to incorporate a negative EBL resist, Hydrogen silsesquioxane (HSQ), instead of PMMA. This change enabled the fabrication of continuous silver films, punctuated by recessed microwell cups containing the single nanohole apertures. Theoretically, in this manner, active surface molecules are able to diffuse along the continuous surface and become confined in the cups more easily than if they had to climb over raised vertical sidewalls to reach the sensor (as they would have if a positive resist process was used).

While both fabrication methods incorporate a similar process flow, the choice of positive or negative electron beam resist directly determines the topography of the silicon template, which, in turn, determines the template-stripped [29] device profile (as seen in Figure 4). Because data from devices using both fabrication methods will presented, an in-depth description of each fabrication process is provided below.

2.1.1 PMMA

The only process flow differences between using a positive photoresist (such as PMMA) and a negative photoresist (such as HSQ) is during the fabrication of the silicon template. To produce our template-stripped resonators, the etched silicon mold needs to match the topography of inverse cups. This means we need to fabricate raised silicon pillars out of the substrate. However, to achieve this using a positive resist etch mask, we would be required to expose and develop the entire surface of electron beam resist, except for the resist covering the pillar profile area. Using electron beam lithography, this would take many hours, and as such was an inefficient use of our resources. As a compromise, we patterned 3 μm-wide rings, with an inner diameter matching the desired diameter of the silicon pillar. This enabled a raised pillar to be etched into the silicon.

While PMMA is capable of acting as an etchmask, it etches quickly using silicon selective recipes. Because of this, while designing the fabrication process, we were afraid that the PMMA alone would not be robust enough to function as an etch mask. Therefore we included a hardmask layer composed of thermally grown silicon dioxide. This layer enabled us to etch the silicon, without compromising the mask integrity mid-etch.

As seen in Figure 4a, a silicon mold template was first prepared by spin-coating a layer of PMMA EBL resist on top of a layer of thermally grown silicon dioxide. The PMMA was about 500 Å thick. Using ellipsometry, the silicon dioxide layer was measured to be approximately 2400 Å thick. The PMMA was exposed using EBL (Vistec EBPG5000+) (Figure 4b).

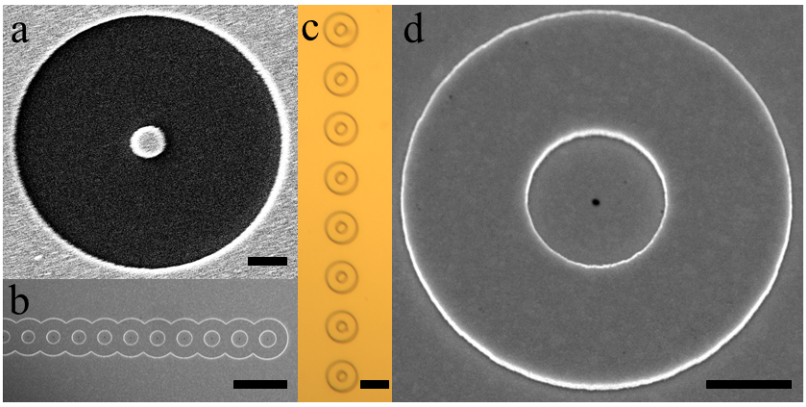

Figure 5: Images of PMMA structures. (a) SEM of PMMA mold after dry etching, but prior to silver deposition. (b) closely packed linear array of structures. Spacing between cup edges is 3 μm. (c) Separated structures. Center-to-center distance for between cups is 25 μm. (d) SEM of template stripped PMMA cup. The raised ring creates a microwell cup in the center. Scale bars: (a) 1 μm (b) 10 μm (c) 9 μm (d) 1.5 μm .

After developing the exposed resist, we used reactive ion etching (RIE) to remove the exposed areas of the silicon dioxide hardmask (Figure 4c). The samples were then exposed to anisotropic deep-trench reactive ion etching (DRIE), using a custom C_4F_8 and SF_6 based recipe (Figure 4d). The SiO_2 etch mask protected the innate atomic smoothness of the polished, <100> crystalline, silicon pillar capital surfaces. The silicon dioxide hardmask was removed using buffered oxide etch (BOE) in a 10:1 ratio (Figure 4e, SEM shown in Figure 5a). Samples were cleaned using a 3:1 (H_2SO_4:H_2O_2) heated piranha bath. A thin film (200 nm) of silver was sputtered onto the prepared, clean template (Figure 4f). Sputtering was chosen over evaporation to improve pillar sidewall coverage on the silicon template. This was followed by using a gallium ion beam to mill an aperture through the top of the silver-coated silicon pillar (that is, through the final device's backside) (Figure 4g). Milling apertures at this point ensures that the silicon/silver interface inside the cup cavity remains uncontaminated and undamaged by excess impinging gallium ions. The beam was manually aligned to the center of the silver-coated pillars to bore ~175 nm apertures. Once the template was fully prepared and milled, we adhered the silver film to a glass slide using optical epoxy (NOA 61). The epoxy was cured by UV-exposure. After curing, the glass slide was stripped from the template, effectively transferring the patterned silver film from the silicon chip to the glass/epoxy substrate. An illustration of the final structure can be seen in Figure 4h.

The PMMA process results in the creation of a cup-like structure, how-

ever the cup is not flush with the rest of the surface. As can be see in the SEM of Figure 5a, the template is formed by etching out a 'doughnut' shape in the silicon wafer. These structures can be constructed close together, in a daisy chain pattern (Figure 5b) or as individual units (Figure 5c). Both configurations produce similar results, and both arrangements template strip equally well. The advantage of closely packing these structures is that a higher density of unique sensory datapoints can be captured at once on a CCD (assuming adequate spatial resolution of the imaging system). Both of these configurations place cups within 25 μm of each other to ensure multiplexed transmission spectra capturing ability. Because the propagation distance of a surface plasmon at optical wavelengths on a silver film is between hundreds of nanometers (short wavelengths) to hundreds of microns (long wavelengths) (Figure 3), and wave confinement is inversely proportional to propagation length, both configurations exhibit the same behaviors. Cups in the closely packed array array have 3 μm of space between cup edges. In the spaced array, that distance is 25 μm. However, due to the changing radius of the cup diameters, the structures are not purely periodic, to prevent formation of periodically coupled plasmon waves on the backside of the structures. Finally, a finished, template-stripped structure is shown in Figure 5d. While we believe that the active optical and plasmonic properties of this structure are nearly identical to those of cups patterned using HSQ (see Figure 6d), the PMMA-based method does not produce a recessed cup structure relative to the surface of the silver film. For many applications this may not be problematic, but the raised sidewalls could impede laminar flow in microfluidic channels, as well as deterring the diffusion of active surface molecules into the cup. In order to avoid these potential shortcomings, a negative photoresist fabrication process should be used, in order to produce recessed cup resonators on the silver film.

2.1.2 HSQ

While there are many options for negative electron beam photoresists, HSQ was chosen for its unique properties post-development. After exposure and development, HSQ becomes very similar in chemical composition to silicon dioxide [30]. This enables us to use patterned HSQ as an etch hardmask, without the need for a second mask layer. The HSQ-based process flow is a simpler version of the PMMA-based process flow, as can be seen by Figure 4. Nevertheless, a description of the HSQ-based fabrication process is given below.

The process for fabricating cup resonators using HSQ is illustrated in Figure 6. A silicon mold template is first prepared by patterning a hydrogen silsesquioxane (HSQ) etch mask via electron beam lithography (Vistec EBPG5000+). Next, we use an anisotropic deep reactive ion etching recipe

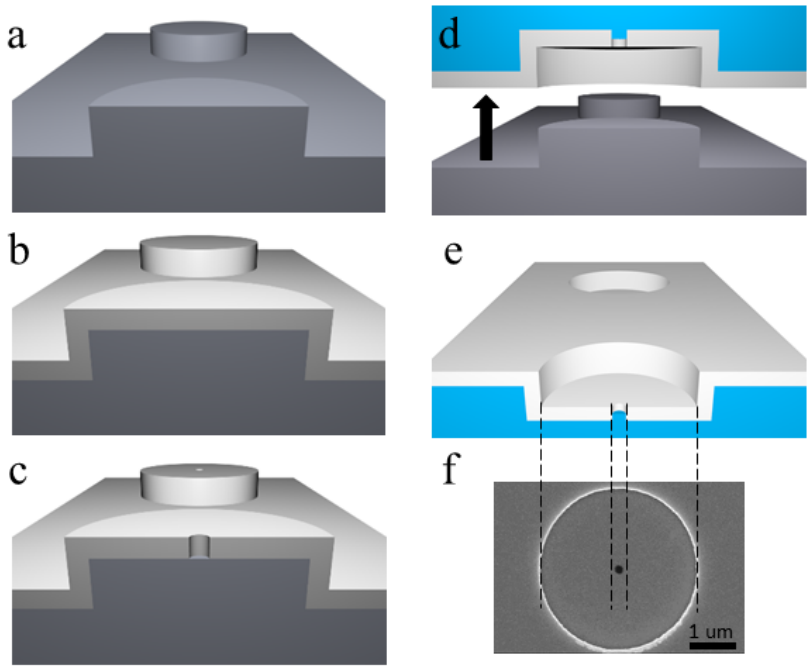

Figure 6: Illustration HSQ fabrication process flow. (a) The silicon template is fabricated using dry etching (b) The mold is coated with 200 nm thick silver via sputtering. (c) A nanohole aperture is milled through the silver from the backside of the structure. (d) Epoxy is applied to the silver layer, and the patterned structure is template stripped from the mold. (e) The final template-stripped structure is shown in reference to (f) a SEM of a completed structure. Scale bar 1 μm.

(C_4F_8 and SF_6 based) to create silicon pillars (Figure 6a). The HSQ etch mask preserves the innate atomic smoothness of the polished, <100> crystalline, silicon pillar capital surfaces. This can be observed in the SEM image of Figure 7a: while the sidewalls are rough, the capital surface of the pillar remains smooth. The HSQ mask was removed using a 10:1 buffered oxide etch, and the sample was cleaned with 3:1 (H_2SO_4:H_2O_2) piranha solution. A thin film (200 nm) of silver was sputtered onto the prepared, clean template (Figure 6b). Again, sputtering was chosen over evaporation to improve pillar sidewall coverage on the silicon template. Figure 7b includes a scanning electron micrograph (SEM) of the sputtered silver coating on the backside of the structure, prior to application of epoxy. The backside film appears visibly rough and the pillar edges are rounded. After sputtering, apertures were milled with a gallium focused ion beam (FEI Quanta 200 3D) through the top of the pillar (or through the final devices backside) (Figure 6c). Milling apertures at this point ensures that the silicon/silver interface inside the cup cavity remains uncontaminated

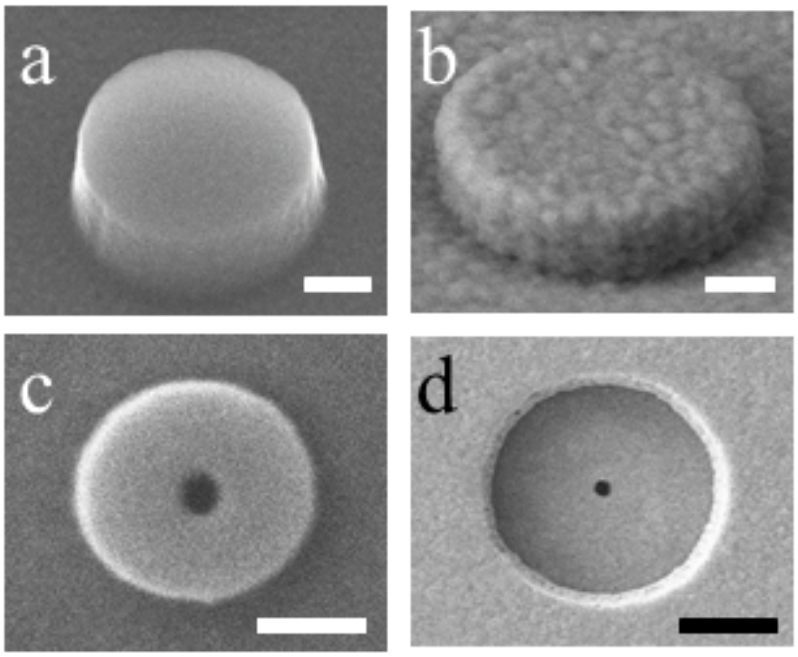

Figure 7: Images of HSQ structures. (a) SEM of HSQ mold after dry etching and removal of etch mask. (b) Mold after silver sputtering. Notice the rough surface of the exposed silver interface. (c) Silver coated silicon pillar after FIB milling aperture. (d) Final device after template stripping. Scale bars: (a) 200 nm (b) 200 nm (c) 750 nm (d) 1 μm .

by excess gallium. The beam was manually aligned to the center of the silver-coated pillars to bore ∼175 nm apertures. An SEM of a milled structure, pre template stripping can be see in Figure 7c Once the template was fully prepared and milled, it was adhered to a standard glass microscope slide with optical epoxy (NOA 61) and cured by UV-exposure. After curing, the glass slide was stripped from the template, effectively transferring the patterned silver film from the silicon chip to the glass/epoxy substrate (Figure 6d). The final, template-stripped structure is illustrated in Figure 6e, where it is directly compared to an SEM of the same structure (Figure 6f). Another SEM of a template structure can be observed in Figure 7d.

In comparison with PMMA, using HSQ directly as an etch mask is a simpler process. Because the resist is able to function as its own etch mask, processing is faster, and due to fewer steps, there are less chances of sample contamination or user error. However, besides the added simplicity, the main benefit of this process is that it creates recessed cups in the in metal surface, which open up many new possibilities for use in biosensing applications.

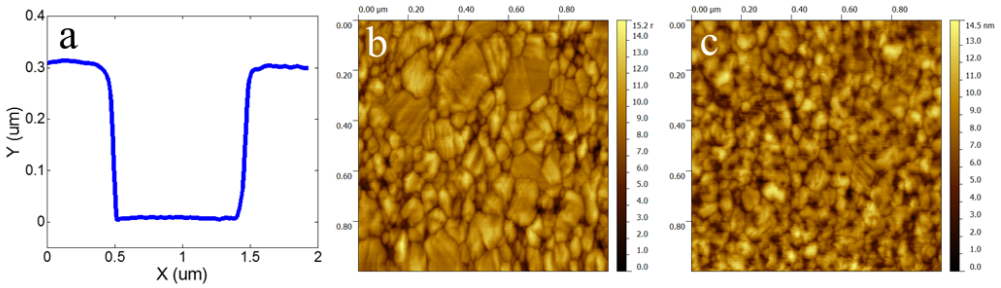

Figure 8: (a) A cross sectional scan of a 1000 nm diameter cup. The cup is approximately 300 nm deep. (b) Topography of deposited silver film inside the cup. Surface roughness is approximately 1.7 nm RMS over a 1 μm surface area, with individual grains possessing surface areas of 0.4 nm RMS. (c) Topography of silver film surrounding the cup. RMS roughness is measured to be approximately 1.84 nm RMS over a 1 μm square. (Data acquired by Luke Jordan) area.

2.1.3 Fabrication Characterization

While various characterization tools were used during fabrication to determine film thickness (Ellipsometry, Profilometry, Reflectometry) and structure dimensions (SEM), analysis of the final structure was performed by atomic force microscopy (AFM). We used AFM to measure cup depth and surface roughness. As seen in Figure 8, we performed both line scans and topographical scans. Figure 8a shows a cross-section through a 1 μm diameter cup. Based on the time spent in DRIE, we expected a cup depth of approximately 300 nm; we were pleased to find that our AFM measurements (Figure 8a) agreed with our estimations. Due to the convolution of the AFM tip with the cup surface and the rapid change in surface profile at the cup sidewall, we cannot use this measurement to precisely determine the sidewall slope, however, qualitatively, they appear to be reasonably vertical. The cross sectional scan also indicates that the surface roughness of the interior of the cup is low. To verify, we performed a surface topography scan of the silver/air interface at the bottom of the template stripped cup (Figure 8b). Using WSxM AFM software [31], the surface roughness of the template stripped cup bottom was calculated to be about 1.7 nm RMS based on a 1x1 μm sample area. An individual $\sim$130 nm grain was measured to have a surface roughness of 0.4 nm RMS. In comparison, the roughness of the silver film surrounding the recessed cup was also measured (Figure 8c). Again for an area of approximately 1x1 square microns, the surface roughness was calculated to be 1.84 nm RMS. However, note that outside the cup, the silver grain sizes are much smaller. Furthermore, while the RMS roughness of single grains inside the cup is $<$0.5 nm, the RMS roughness for similarly sized regions outside the cup is $>$2.0 nm. The

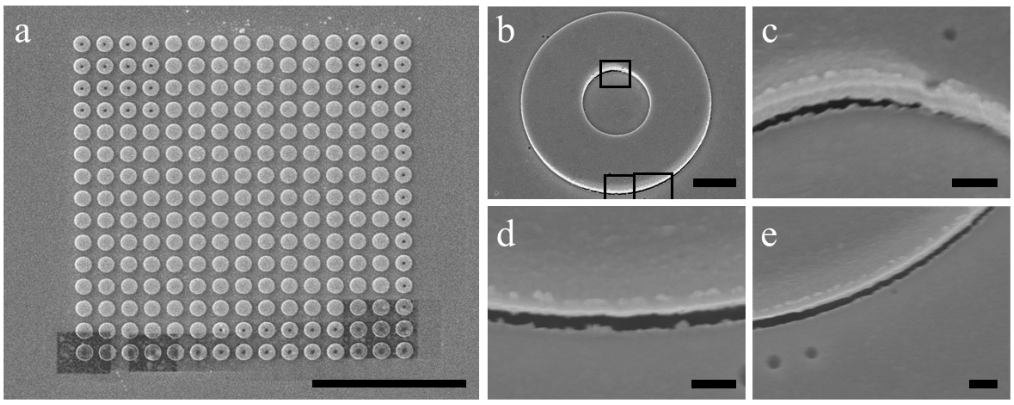

Figure 9: Some common issues in fabrication. (a) Over exposure by FIB damages the structures. Notice the clean apertures milled in the top left corner of the HSQ mold array. (b) SEM of a template stripped PMMA cup. Boxes show insets and correspond to parts c, d, and e in a counter clockwise direction. (c,d,e) SEM images showing tearing and separation of the cup resonator structure caused by template stripping. Scale bars: (a) 10 μm (b) 1 μm (c,d,e) 300 nm.

larger (and smoother) grain sizes inside the cup are due to the atomic smoothness of the polished silicon on which the silver is deposited. Low surface roughness is important inside our structure because it improves the dielectric function of the metal for use in plasmonic applications [32]. The major contributing factor to surface roughness inside the cup are the grain boundaries: if these could be removed or smoothed, the surface roughness would decrease even further. However, sputtering is currently purged to a vacuum pressure of $\sim 1.2 \times 10^{-6}$ Torr. While the chamber is prepped to high-vacuum, there still molecular containments (primarily water) present in the chamber [33]. These conditions were used for all measured samples, to ensure uniform thickness between device sets, in an attempt to mitigate thickness-dependent nanohole transmission resonances [34]. These samples were also not annealed. Roughness might be decreased by increasing the substrate temperature and/or the argon sputtering pressure (currently we use 5 mTorr) [35]. Despite these shortcomings in metal deposition, the surfaces still support the build up of plasmon resonances inside the cup, enabling modulated light transmission through the nanohole.

Nevertheless, as with many deposited thin films, surface roughness could be decreased further by increasing grain sizes and reducing grain boundaries through heated deposition or annealing. This improvement might also increase the propagation length of surface waves in the structure, leading to strengthened standing waves and thus increased transmission enhancement through the nanohole aperture.

Because these devices enhance optical transmission through a nanohole using reflected surface plasmons, it is imperative that the geometry of the structure is without defects. However, it is easy to damage these structures in the fabrication process. As seen in Figure 9 there are two primary sources of error during fabrication.

During FIB milling, the ion beam is manually aligned to the center of each pillar to mill each aperture. However, during alignment, the entire field of view is bombarded with low doses of Ga+ ions, while the aperture receives a more concentrated dose during milling. If the alignment takes too long, or the viewing magnification is too high, the silver film can receive a damaging dose of Ga+ ions. If this occurs, the cups can suffer permanent performance degradation. Figure 9a shows an example of well milled apertures (in the top left corner) in comparison with damaged cups (at the bottom of the array). While this error can be mitigated with careful planning and operation of the FIB tool, devices can also fail during the final template stripping step.

If the adhesion of the metal is too strong to the silicon, devices will not template strip. Although the sidewalls are vertical, they are capable of template stripping without difficulty. However, in some cases the sidewalls become detached from the bottom surfaces of the cup resonator. This can be caused by extra thin silver at the edges, (from extended exposure in the FIB wearing down the silver or poor step coverage during sputtering), or by using poor technique while template stripping. As can be seen in Figure 9b-e the silver sidewalls have become detached from the cup structure. Both of these tears occur on the bottom edge of the raised sidewalls, indicating that the chip was template stripped perpendicularly to both tears. Tears like this will decrease the signal to noise ratio in the transmitted data by both transmitting white light through the tear, while also disrupting the plasmon resonances in the structure.

2.2 Measurements and Spectroscopy

To demonstrate how the cup radius affects optical transmission through the milled nanohole, we fabricated sets of devices with radii varying from 225 nm to 2425 nm in 50 nm increments (similar to those shown in Figure 5b-c). Three example spectra for different cup radii are shown in Figure 10. This figure also illustrates the two illumination schemes for the structures, and includes resulting spectra from both schemes. SEM images in Figure 10 show the nanohole diameters for these datasets are approximately 175 nm. From previous SEMs (e.g. Figure 7), the sidewall thicknesses are estimated to be between 50 and 60 nm. The HSQ-based dataset from which Figure 10c,e were selected was collected in January/February of 2015, and will be the primary dataset discussed in this thesis. Previous datasets have

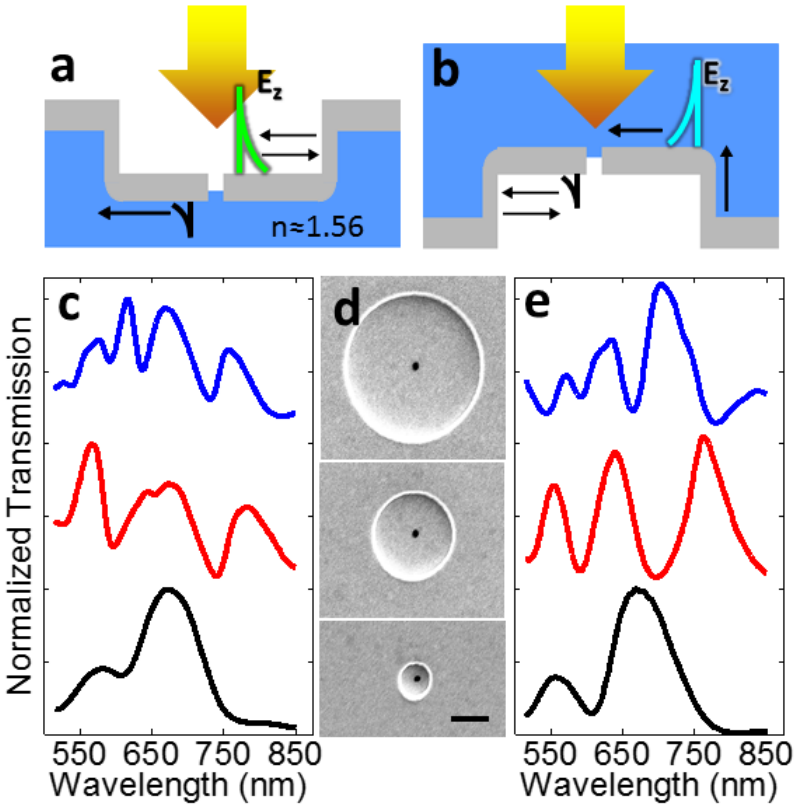

Figure 10: Representative transmission spectra from the same structures using cupside and backside illumination. (a) Cup-side illumination. Highly enhanced electric fields inside the cup produce dominant resonance. (b) Epoxy-side illumination. Electric fields are enhanced on the backside of the structure. The dominant resonances is on the backside of the cup. (c) Transmission spectra from cup-side illumination. (d) The radii of cups are estimated to be 1900, 1025, and 415 nm respectively. Micrographs are scaled such that the scale bar for all three micrographs is 1 um. (e) Transmission spectra from epoxy-side illumination.

similar characteristics, so for simplicity and consistency, the 2015 set will be backdrop on which our analytical models will be presented.

Due to the acquisition of new equipment in our laboratory, several light sources and spectrometers were used to measure our data over the course of this research. However our most recent measurements were conducted using a fiber-coupled, laser-driven light source (Energetiq, EQ-99FC); this source was used to illuminate the cup resonators through a 600 mm long fiber, reflective collimator, and condenser on top of an inverted microscope (Nikon Ti-S). While the exposed cup side of the device will be most useful for sensing applications, in order to develop a more thorough understanding

Figure 11: Collection process walkthrough. Cups were backside illuminated, and show some light leakage through the structures. (a) Live image of the structures to be measured. There seems to be some light leakage around the edges of the sample. Apertures were round, the teardrop shaped transmission is an artifact caused by oversaturating the CCD. (b) Although there was some light leakage through the structure, by narrowing down the spectrometer slit, we are able to multiplex light collection from only the center nanohole apertures of the devices. (c) An unprocessed image of the resulting device spectrum. During post-processing we were able to select the centers of the spectrum, eliminating distortion from scattering at the edge of the structure.

of device behavior, transmission spectra were measured using illumination from both sides of the sample: cup-side measurements were gathered using illumination from above the structure, directly onto the air/silver interface (Figure 10a), while back-side measurements were gathered using light which propagated through the glass slide and epoxy layer before impinging on the silver/epoxy interface at the bottom of the cup (Figure 10b). Transmitted light was collected with a 50x, 0.9 NA objective and imaged onto the entrance slit of a 300 mm focal length imaging spectrometer (Acton SP2300i) equipped with a back illuminated, deep depletion thermoelectrically cooled CCD (Princeton Instruments PIXIS 400B). Multiple cups were imaged onto the entrance slit, effectively multiplexing data collection. Spectra were background subtracted and normalized to transmission through the glass substrate. Figure 11 shows an example of our collection process.

When illuminated on the cupside, transmission is dominated by plasmons coupled to the air/silver interface inside the cup. Conversely, in backside illumination the dominant transmission features originate from plasmons on the epoxy/silver interface. In both cases, as the cup radius is increased, we observe an increase in the number of resonant peaks. Representative transmission spectra, from the same strutures, using both cupside and backside illumination, are presented in Figure 10c and 10e. SEM micrographs of the measured cups are displayed between them (Figure 10d).

While all datasets share similar characteristics, device performance var-

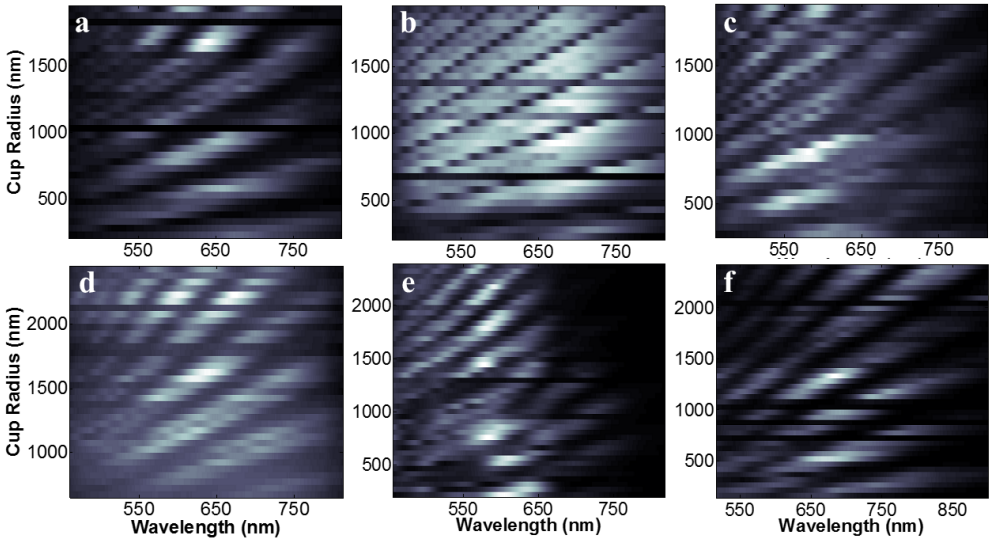

Figure 12: Backside illumination transmission spectra contour plots for 6 different samples. (a) HSQ cups measured Nov 2013. Cup depth 450 nm. (b) PMMA cups measured Oct 2013. Cup depth is 400 nm. Aperture diameter 160-170 nm. (c) PMMA cups measured Nov 2013. Cup depth 500 nm. (from same silver deposition as 'a')(d) HSQ cups measured Nov 2013 (from same process run as 'a'). Cup depth is 450 nm. (e) HSQ cups measured May 2014. Cup depth 400 nm. Aperture diameter 180 nm. (f) HSQ cups measured Jan 2015. Cup depth 300 nm. Aperture diameter 180 nm.

ied somewhat from chip to chip, due differences in fabrication, primarily assumed to be differences in device symmetry, nanohole size and placement, and silver quality, thickness, and roughness. The spectral differences between various fabricated device sets are shown in Figure 12. All spectra in this figure were collected using backside illumination. The spectra are arranged in the form of contour plots to easily visualize the relationship between transmission wavelength and cup radius. Each horizontal row of the plot displays the transmission spectrum of a single cup resonator (corresponding to a radius listed on the y axis). Transmission spectra are aligned with wavelengths listed on the x-axis. Dark rows are defective cups. Maximum transmission is represented by white, minimum is represented by black. All spectra were background subtracted and normalized to the light source and each contour plot is normalized to the maximum transmission value for that dataset. All datasets demonstrate a spectral redshift with increasing cup radius. The silver films utilized in Figure 12a,c-d were deposited together in parallel, under the identical conditions. Despite this, it is immediately obvious that the peak and dip widths are different for each

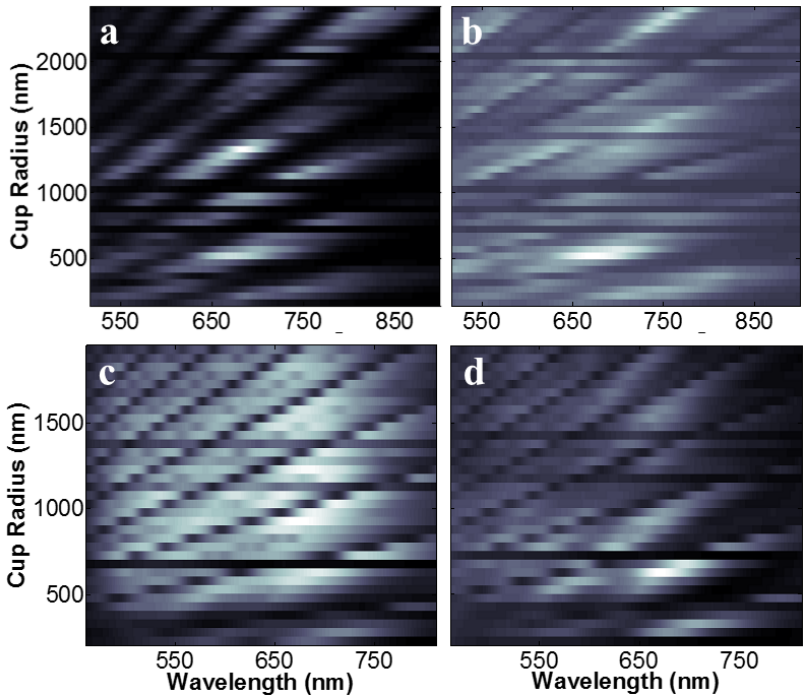

Figure 13: Transmission spectra contour plots of both Backside and Cupside illumination for two different samples. (a) Backside illumination for January 2015 HSQ sample. (b) Cupside illumination for January 2015 HSQ sample. (c) Backside illumination for Oct 2013 PMMA sample. (d) Cupside illumination for Oct 2013 PMMA sample.

of these datasets. As stated previously, these difference are attributed to difficult to-control-differences in cup fabrication. Figure 12a,d-f are all HSQ cups, while samples shown in 12b-c were template stripped from PMMA molds. While the HSQ cups all produce similar looking contour plots, the PMMA cups obviously appear differently. For all sets, notice that there are two distinct sets of broad and narrow lines cutting through the field. Narrow lines are seen prominently in 12b, while the broad lines are easily observed in 12a,d-f. The difference between these two interference patterns will be discussed late in this text.

Complimentary cupside illumination data was not collected for all of the sample measurements shown in Figure 12. However in Figure 13 we show both cupside and backside illumination for two datasets, corresponding to Figure 12f (the 2015 HSQ set, previously featured in Figure 10, and Figure 12b (a 2013 PMMA set), As can be seen, in the HSQ cups, broad dips are only present during backside illumination (Figure 13a), while cupside illumination features narrow transmission dips (Figure 13b). There is a difference in refractive index between epoxy and air. We believe that this causes the difference in slope between broad interference dips and the

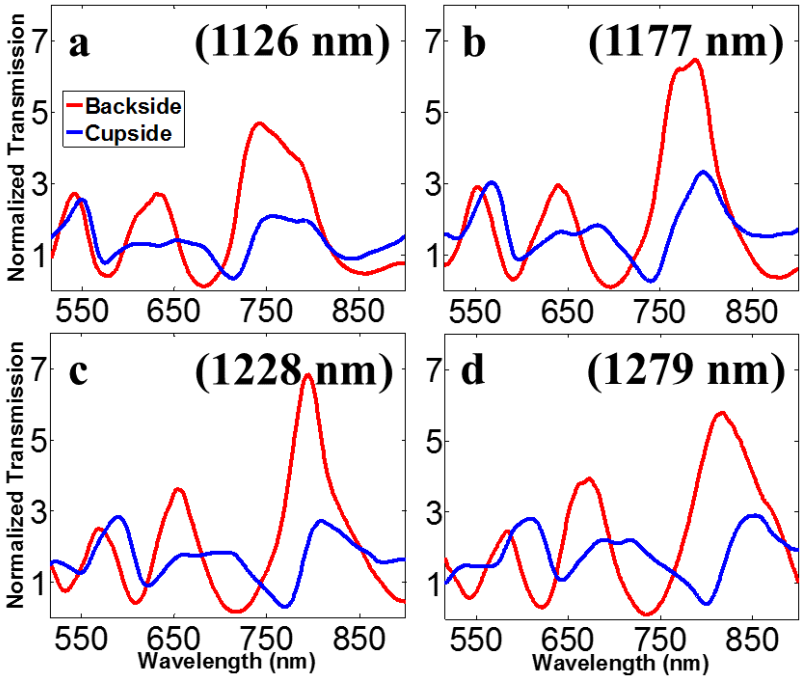

Figure 14: Cupside and backside transmission from the January 2015 sample, normalized to transmission through identically sized un-cupped nanohole apertures on the same chip. The radius of each cup is listed in parentheses. Observe the red-shifting of the peaks and dips with increasing cup radius. Both cupside and backside illumination tend to show a 3-5x enhancement over single nanoholes in the visible spectrum. These 4 consecutive cup sizes were particularly chosen due to the high contrast between peaks and dips observable in data from both illumination schemes.

narrow interference dips, indicating that resonances are dominated by plasmons on the illuminated face of the structure.

However, the PMMA cups do not show distinctive differences between cupside and backside illumination. Upon careful inspection of Figure 13c it can be seen that between dark dips, there are lighter gray intermediate dips. These suggest that plasmons are being generated at the edge of the cup, as opposed to generation at the nanohole, which would be indicative of light leakage through a defect similar to the ones illustrated in Figure 9b-c. This theory somewhat aligns with raw experimental data: Figure 11 shows that some samples may have had some light leakage present. Furthermore, there is little to no indication of any resonances originating on the backside of the device, which would be illustrated by the presence of steeper, broader dip trends - like those present in Figure 13a. A backside edge defect may have prevented backside resonances from modulating transmission or perhaps the backside surface was prohibitively rough. In any case, the internal

resonances dominated for both backside and cupside measurements, an effect which we have not been able to reproduce in any other samples.

Both cupside and backside illumination results in enhanced transmission through the nanohole. Figure 14 shows 4 sets of paired cupside and backside spectra from the January 2015 HSQ data. Unlike the previously shown data, these spectra were normalized to un-cupped nanohole apertures milled into the silver film alongside the cupped apertures. These 4 consecutive cup sizes were chosen due to the high contrast between peaks and dips observable in data from both illumination schemes. The radius of the cup is listed in parentheses. We observe that backside illumination generally results in a greater enhancement, however both illumination schemes result in at least 3x enhancement versus an un-cupped nanohole. The increased enhancement from backside illumination is believed to be caused by higher index of refraction in the optical epoxy layer, which effectively increases the numerical aperture of the nanohole, allowing more light to transmit. This could be tested by introducing an index-matched fluid into the cup and repeating measurements.

2.3 FDTD Simulations

We performed 2D finite-difference time-domain (FDTD) simulations of our cup resonator structures. To closely match the physical geometry of the devices, we incorporated 1600 nm radius, 300 nm cup depth, 170 nm aperture, 200 nm thick silver film coverage, and 50 nm thick sidewalls. Modeling was performed using Lumerical FDTD Solutions. The dispersion of the dielectric function of silver was incorporated using a Drude-Lorentz model fit to experimentally measured values. A total-field scattered-field plane wave light source was used to illuminate the structures. Simulations cover a slightly larger wavelength range (400-900 nm) than our experimental datasets, and were allowed to run until 0.001% of the initial excitation energy remained in the modeling area. The modeling volume was kept constant for all simulated cups. Perfectly matched layer (PML) boundary conditions were used in all directions. Due to the relatively large radial dimensions of our structures, we do not observe vertical cavity optical resonant modes in our simulated structures [26].

Simulated transmission spectra (2D) resulting from cupside and backside illumination of the 1.6 m radius cup are shown in Figure 15a. Due to the TM polarized nature of the surface plasmon wave, we generated magnetic field (H_y-component) maps (Figure 15b) using cup-side illumination. We selected wavelengths corresponding to points of simulated minimum and maximum transmission; these are marked with dashed lines in Figure 15a. We chose to display the real component of H_y to illustrate far field behavior of transmitted light, and plotted $|H_y|^2$ to demonstrate how stand-

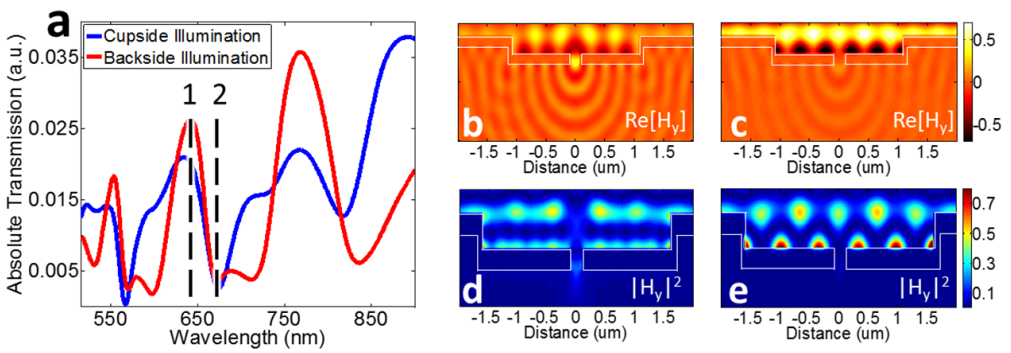

Figure 15: FDTD simulations for a single cup resonator. The featured cup has a 1600 nm radius, is 300 nm deep, and utilizes 200 nm thick silver films with 50 nm sidewalls. Hz-component field maps are generated for wavelengths of 640 nm (b,d) and 670 nm (c,e). (a) Transmission spectra from both cupside and backside illumination are plotted. Dashed lines indicate transmission peaks and dips. (b) Re$[H_y]$ mapping demonstrates a standing wave anti-node at the nanohole, leading to cohesive propagating wavefronts at transmission maximum. (c) Re$[H_y]$ mapping demonstrates a standing wave node at the nanohole, weakening the wavefronts propagating away from the nanohole at transmission minimum. (d) Transmission enhancement is caused by a standing wave constructive interference at the nanohole, allowing plasmons to couple into the aperture. (e) Transmission minimization is caused by a standing wave deconstructive interference at the nanohole, preventing plasmons from coupling into the aperture.

ing wave resonances inside the structure determine transmission intensity. We observe that at wavelengths of maximum transmission, the real component of H_y forms cohesive wavefronts propagating away from the aperture. However, at a transmission minima, because of deconstructive interference at the nanohole, these propagating wavefronts become blurred and weaker in intensity.

The mechanism of optical transmission through the subwavelength nanohole aperture can be understood by looking at plots of $|H_y|^2$ in Figure 15b. During maximum transmission, we observe that fields in the nanohole are excited, while at minimum transmission there is very weak field coupling in the aperture. Simultaneously, during maximum transmission, we observe that the standing wave plasmon resonances inside the cup are much weaker than their minimum transmission counterparts. Thus, during peak transmission, propagating plasmon waves are coupling into the nanohole, in turn reducing the intensity of the standing wave in the resonator cavity. The opposite occurs during minimal transmission.

Therefore, it follows that if the resonant standing wave has a node at the nanohole, propagating plasmon waves will deconstructively interfere at

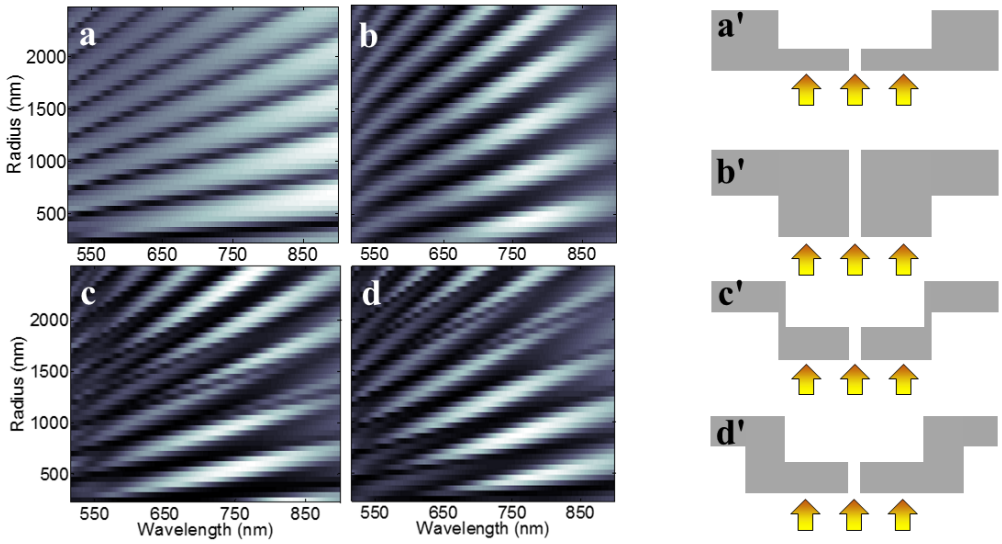

Figure 16: Simulated transmission intensity contour plots using epoxy-side illumination. The cup radius is varied from 250 nm to 2500 nm. Cross sections of the structure are tagged with an identical primed figure label. (a, a') Contour plot of cup resonator structures with infinitely thick sidewalls. (b, b') Contour plot of a zero-radius cup with thick sidewalls, observing only resonances due to the topography of the backside structure. (c, c') Contour plot of cup resonators with 50 nm thick sidewalls. (d, d') Contour plot of cup resonators with 250 nm sidewalls. Notice the peak/dip red-shift with increasing shelf length.

that point, disenabling them from coupling into the aperture. Conversely, if the standing wave has an anti-node at the nanohole, propagating plasmons will constructively interfere and couple into the nanohole, thus enhancing transmission through the subwavelength aperture [36]

These same behavioral trends apply to plasmons resonating on the epoxy/ silver interface during backside illumination. We observe in Figure 15a that peaks and dips occur at approximately the same wavelengths during backside illumination as those measured using cup-side illumination. However, backside illumination also results several additional dips, which we believe are caused by backside plasmon standing wave nodes at the nanohole aperture. Backside illumination transmission dips coincide with cupside dips because the same resonant plasmon modes are excitable with both illumination schemes. Because the cup resonator has highly reflective mirrors surrounding the aperture, plasmons are easily confined on the air/silver interface, as compared to the non-reflecting rounded bottom edge on the backside of the structure. This is why cup-side resonance conditions dominate the transmission behavior of the device.

To verify that backside plasmon resonances also modulate transmission through the nanohole, we simulated 2D cup resonators with infinite, 50 nm, and 250 nm thick sidewalls, as well as a zero-radius cup with increasingly thick sidewalls (Figure 4a'-d'). Simulations were performed using backside illumination. The transmission intensity of light through the nanohole is dependent on both illumination wavelength and cup radius. To visualize the relationship between these three variables, we constructed transmission intensity contour plots as seen in Figure 16a-d. The letter label associated with each section of the figure matches the primed label illustrating the structure being simulated.

Infinitely thick sidewalls eliminate transmission modulation from back-side resonances, as there are no discontinuities on the backside to excite plasmons back towards the nanohole aperture. In this scenario, a simple interference relationship inside the cup is observed (Figure 16a,a'). Inversely, to simulate transmission modulation through the nanohole caused only by back-side resonances, we modeled a zero-radius cup with increasing sidewall thickness (equivalent to a solid silver pillar containing a single aperture), thus eliminating the cup-side resonances ((Figure 16b,b')). Due to the epoxys larger refractive index, an increased slope in the interference pattern for back-side resonances is observed. Interference patterns from cup-side (Figure 16a,a') and back-side (Figure 16b,b') resonances are both present in the simulation of the fabricated structure (Figure 16c,c'). To verify that these enhanced interferences were not due to plasmons coupling through the 50 nm sidewalls [37], we also simulated optically thick, 250 nm sidewalls (Figure 16d,d'). Increasing the backside plasmon cavity surface length by thickening the sidewall caused the resonant plasmon wavelengths to redshift, while leaving the cup-side resonances unchanged. These simulations verify that plasmons on both sides of the structure modulate transmission through the nanohole. Since the penetration depth of an electric field into silver is approximately 25 nm at optical frequencies, we believe 50 nm thick sidewalls are sufficiently thick to act as mirrors for propagating plasmons inside the cup, with minimal interference from active plasmons on the epoxy side of the film.

2.4 Analytical Model

During cup-side illumination, surface plasmons polaritons are excited at the nanohole on the smooth air/silver interfacial surface of the cup base. From the nanohole, plasmons propagate radially outward on this surface and are reflected back towards the nanohole by the silver sidewall mirrors. The plasmons may then couple into the nanohole, enhancing transmission through the aperture. Alternatively, in epoxy-side illumination, plasmons are excited at the rounded edge on the bottom of the backside sidewall

coating. We also observe effects which suggests plasmons are excited at the edge at the top of the backside sidewall. These plasmons then propagate down the sidewall, over the rounded edge of the silver film, and eventually interfere with transmission through the nanohole.

Obviously, for sensing applications, we must track cupside resonances in order to probe changes in the sensing volume. Based on our previous results, using cupside illumination mitigates modulation by backside resonances, only showing transmission interferences generated from resonances inside the cup. Therefore with this illumination scheme in mind, we begin the following analysis. Inside the cup, a first order approximation assumes

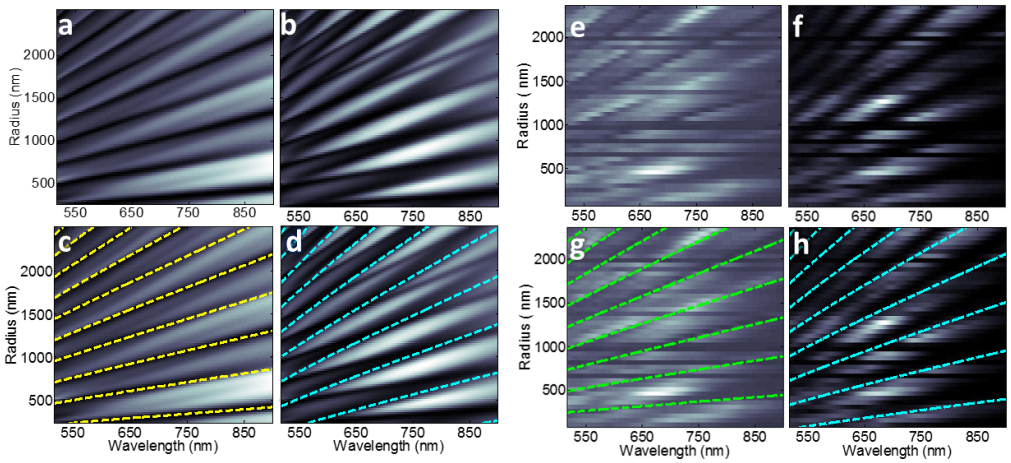

Figure 17: (a,b) Contour plots of 2D FDTD simulated transmission through the nanohole using (a) cup-side and (b) epoxy-side illumination. (c,d) Contour plots of simulated transmission spectra for increasing cup radius, with analytical phase interference fits (color-coded to match electric fields illustrated in Figure 3a and 3b) (e,f) Contour plots of measured transmission spectra through the nanohole using (e) cup-side and (f) epoxy-side illumination. (g,h) Contour plots of measured spectra through fabricated structures for increasing cup radius, with analytical phase interference fits (color-coded).

that surface plasmon polaritons propagate to and from the nanohole with only a single reflection from the sidewall. Depending on losses accrued during reflection and through propagation, there may be multiple reflections. We find a first order approximation useful for qualitatively interpreting our results. Assuming a single round trip path from the nanohole to sidewall and back, the phase of the propagated wave upon return to the nanohole is estimated by:

$$\theta = 2 \times \frac{2\pi}{\lambda_0} \sqrt{\frac{\epsilon_m \epsilon_m}{\epsilon_m + \epsilon_d}} (R + \delta R) + \phi \tag{2.4.1}$$

where ϕ is the phase accumulation (relative to initial phase) through propagation and reflection, λ_0 is the free space wavelength of the illuminating light, $\sqrt{\frac{\epsilon_m \epsilon_m}{\epsilon_m + \epsilon_d}}$ is the effective refractive index of the surface plasmon (n_{spp}),ϵ_m and ϵ_d being the permittivities of the metal and dielectric respectively, R is the radius of the cup structure, δR is the wavelength-dependent electric field penetration depth into the silver mirror, and ϕ is an effective phase shift from reflection. Since we are concerned with only the relative phase shifts of the propagated and reflected plasmon wave at the nanohole, we are do not account for phase shifts caused by plasmon generation or scattering. Assuming an effective phase shift of π (based on the known phase shift caused by reflection from a metal mirror), we estimate that deconstructive interference ($\theta = [2m-1]\pi$) at the nanohole occurs when

$$R = \lambda_{spp}\frac{(m-1)}{2} - \delta R \qquad m = 1, 2, 3...etc \tag{2.4.2}$$

and constructive interference ($\theta = [2m]\pi$) occurs when

$$R = \lambda_{spp}\frac{(2m-1)}{4} - \delta R \qquad m = 1, 2, 3...etc \tag{2.4.3}$$

where λ_{spp} is the surface plasmon wavelength, $\frac{\lambda_0}{n_{spp}}$.

These analytical equations nicely describe the phase shifts that we observe in both the simulation and experimental datasets. As was described above, if the standing wave has a node at the nanohole, plasmons deconstructively interfere at that point, and we observe a dip in the transmission spectra. Oppositely, if the standing wave has an anti-node at the nanohole, plasmons constructively interfere, and we observe a peak in the transmission spectra. These physical interpretations of our experimental and physical datasets agree with the analytical model presented. Deconstructive interference analytical fits are plotted (in green) over the cup-side illumination transmission spectra contour plots in Figure 17e and 17g. A similar analysis can be used when illuminating from the backside of the structure. When illuminating from the backside, we observed the emergence of a second set of deconstructive resonances. Through simulation, we were able to determine that these were caused by plasmons on the epoxy/silver interface on the backside of the cup structure. We assume plasmons are generated at discontinuities on the backside of the structure, namely, the nanohole aperture, the rounded bottom edge of the backside sidewall, and at the $\sim$ 90-degree top edge of the backside sidewall. We believe that due to the inherent roughness of the backside sputtered silver and poor reflection

from backside rounded edge, any plasmon originating at the nanohole will have difficulty propagating away, reflecting, and returning to the nanohole. However, it remains plausible that plasmons generated at either of the discontinuous backside edges would be able to propagate to the nanohole and interfere with transmission. In this case, the phase interference equation is modified:

$$\theta = \frac{2\pi}{\lambda_0}\sqrt{\frac{\epsilon_m \epsilon_m}{\epsilon_m + \epsilon_d}}(R + L + H + \delta R) \tag{2.4.4}$$

where L L is an additional path length composed of the thickness of the sidewall, while H represents the sidewall height. This modified analytical model for backside illumination appears to fit well with our simulated and measured data, while equations describing round trip plasmon interference do not. Notice that there is no reflected phase shift - since plasmons are not reflecting off sidewall mirrors, this term has been removed. Figure 18 illustrates two possible fits using equation 2.4.4. The fits shown here assume no additional phase shifts caused by reflection, as equation 2.4.4 only accounts for phase shifts due to propagation. Assuming these conditions, we observe that the best fit curves are from plasmons which are modeled to have propagated down the backside sidewall. These plasmons could be aided over the rounded edge by source wavefronts propagating away from the device after reflecting on the silver film. These reflected wavefronts could have also excited plasmons at the rounded backside edge after reflecting off the silver film, incorporating an added propagation phase to the surface plasmon [38].

The epoxy used for template stripping has an index of refraction between 1.53 and 1.56 in the visible regime. This causes the surface plasmon wavelength on the silver/epoxy interface to blueshift (relative to surface plasmons on the silver/air interface), explaining the increased slope of the epoxy-side interference patterns in our transmission contour plots. The destructive interference mode fits ($\theta = [2m-1]\pi$) for these backside resonances can be described:

$$R = \frac{\lambda_{spp}[(2m-1)\pi]}{2\pi} - (L + \delta R) \qquad m = 1, 2, 3...etc \tag{2.4.5}$$

For simplicity, we plotted a possible destructive interference fit over simulated and measured transmission contour plots in figure 17a and 17b. We used only one component of the resonant backside plasmon wave, assuming a value of 250 nm for L and 300 nm for H for the simulated structure (simulated sidewalls are 250 nm thick, 300 nm tall), and 50 nm for L and 300 nm for H for the measured structure (actual devices have sidewalls about 50 nm thick, 300 nm tall). We used wider structures for this figure

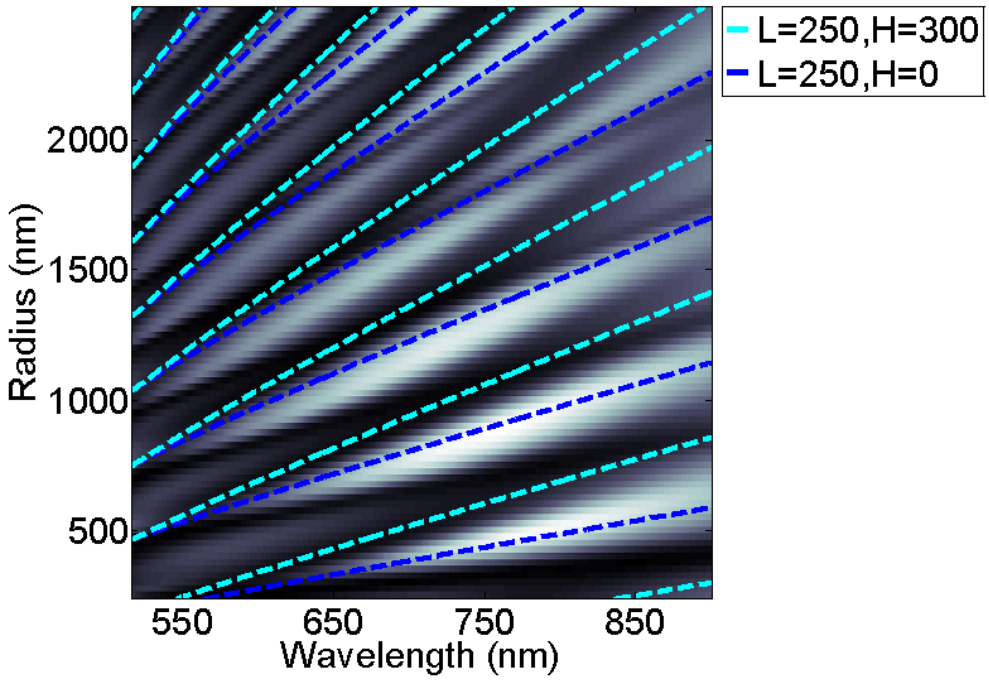

Figure 18: Simulated transmission contour plot with two analytical fits for backside interference. Cyan represents surface plasmons originating at the top of the backside sidewall, while blue represents only those surface plasmons generated at the backside rounded edge. The narrow, flatter dark interference lines are caused by resonances inside the cup. These fits assuming no additional phase shift (i.e. caused by reflected plasmons returning to the nanohole).

for cosmetic reasons (because they were higher resolution simulations) as well as to illustrate that the equations hold for varied sidewalls.

By incorporating sidewall mirrors, we enable constructive plasmonic interference at the aperture; this allows us to enhance transmission through the nanohole plasmon confinement inside the structure. This allows the buildup of standing wave resonances, which have the ability to enhance transmission through the nanohole. Based on FDTD simulations, we believe 300 nm tall silver sidewalls provide about 60% reflectance of propagating surface plasmon polaritons. If the sidewall height is increased to 1000 nm, this reflectance could increase to about 97%, while doubling transmission intensity. Nevertheless, with our current 300 nm tall sidewall,we observe a transmission enhancement of 3-4 times in the visible regime and up to 10 times in the near infrared as seen in Figure 14.

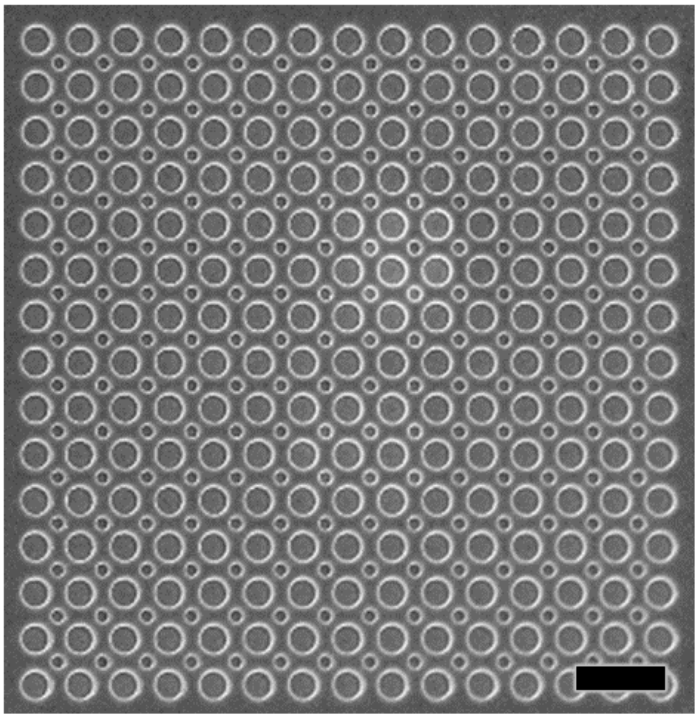

Figure 19: SEM of an unmilled, template stripped high density cup resonator array, illustrating the capability of densely packing multiple sized cups into the same area. Scale bar is 3 μm.

3 Applications, Improvements, and Future Work

Since each nanohole functions as an independent sensor, the reduced footprint of the cup resonator makes it an ideal structure for high density array biosensing. Because the sidewalls confine propagating plasmon waves, there is little worry about interference between structures. We have fabricated 1 m diameter cup resonator arrays with sensor densities 4 times higher than we previously reported using Bragg mirrors [39]. Sensor density can be increased further, to 8 times higher than previously reported, by interspersing large cups in the array with small ones as seen in Figure 19. Figure 20a shows a 11x11 cup resonator array along side a brightfield image of the transmission through the structure (Figure 20b). Notice how the color and intensity of the transmitted light changes depending on the nanohole aperture size, shape, and position in the cup. Although discussed in section 2.1, fabrication errors such as misaligned or faulty apertures, can be clearly correlated with weak signal in this direct comparison.

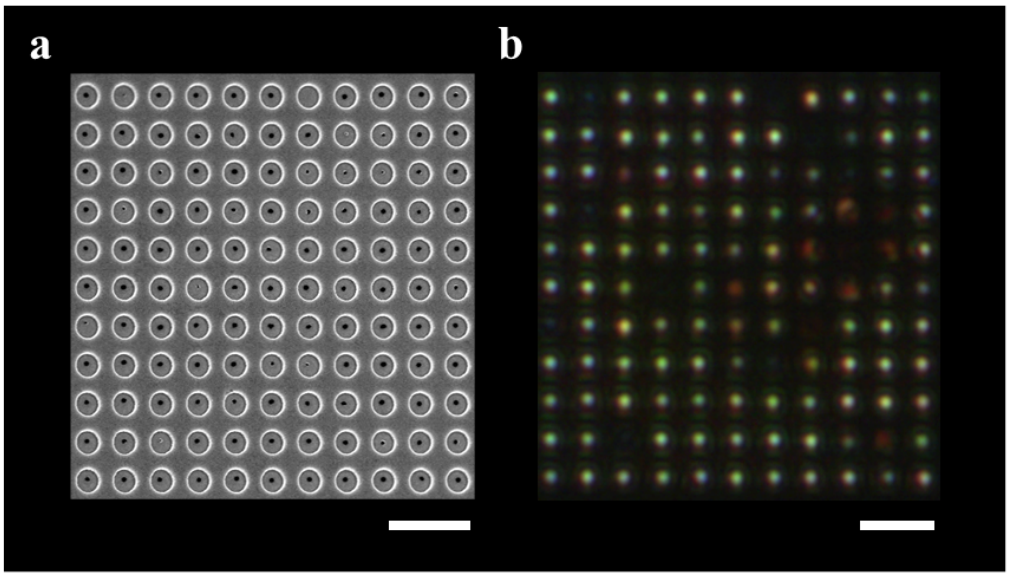

Figure 20: SEM of milled and template stripped high density array compared with brightfield image of the backside illuminated structure. (a) Manually aligned apertures are not directly in the center of the structure, and the FIB does not always mill through the silver. (b) Brightfield image of the structure shown in 'a'. Notice the color and intensity of transmitted light in comparison with the aperture size and placement in 'a'. Scale bars: (a) 3 μm, (b) 3 μm.

Additionally, devices fabricated with sub-micron diameters exhibit resonant transmission at only one or two wavelengths. This causes such devices to emit characteristic colors when illuminated with a white light source. These colors can be observed when viewing the devices through an optical microscope. Bright-field images of the illuminated cups were recorded using a color CCD camera (Thorlabs DCC1645C). In Figure 21, we present transmission spectra of small cups alongside bright-field images of the corresponding structure under illumination. These cups are illuminated from the backside, from the January/February 2015 HSQ dataset. Red shifts in the transmission spectra correlate with visible redshifts in the bright-field images. The blue color of the 400 nm cup is due to a transmission resonance outside the region of our spectral analysis. For cups above 1 m in diameter, multiple resonant transmission peaks cause the cups to emit more neutral, white light colors and therefore they are not displayed here. This data suggests that these devices could be used in color related applications. The data presented in both Figures 20 and 21 indicates that intensity based sensing applications are also possible with these sensors, assuming proper calibration of sensors and high quality devices.

Figure 22 shows a 3D FDTD simulation using two different sidewall

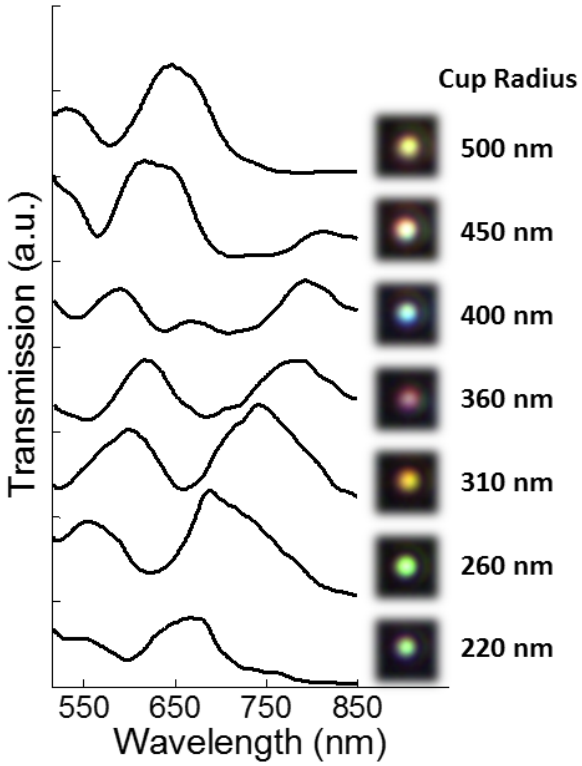

Figure 21: Backside illumination transmission spectra coupled with bright-field images of the cup resonator structures. By altering the radius of the cup structure it is possible to tune the emitted wavelengths, resulting in the transmission of characteristic colors. Small cups have distinct colors due to fewer resonant wavelengths being transmitted.

heights. As can be seen, increasing the sidewall height to 1000 nm from 300 nm results in a transmission enhancement of 1.5-3 times. However, while easily simulated, the fabrication of such deep structures is more complicated than shallower 300-500 nm structures. Etch masks are required to be thicker, greater care is needed to ensure sidewall step coverage in sputtering, and template stripping needs to be performed with proper technique. Deeper structures are harder to template strip due to their taller vertical sidewalls. These structures are not impossible to fabricate, however, but for simplicity, to this point we have mainly focused on shallower structures in the 300-500 nm deep range.

Because of their independent sensing capability and unique 'microwell' shape, cup resonators could prove to be useful sensing tools for biomaterials. Figure 23 illustrates the well volume for three different sidewall heights. Each cup is capable of containing a volume of solution on the order of femtoliters. Because we have demonstrated the ability to fabricate arrays of

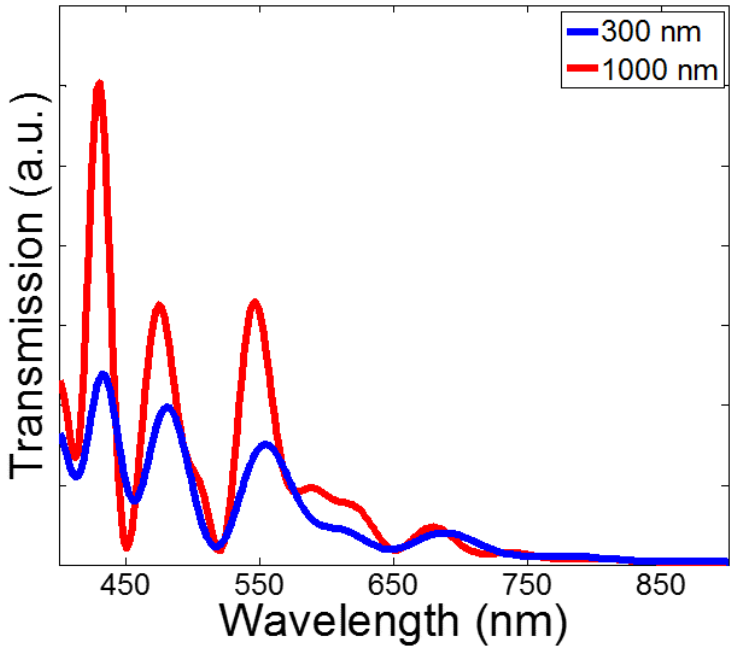

Figure 22: 3D FDTD simulations for infinite sidewall cup (to reduce simulation time due to memory constraints). These simulations indicate that transmission enhancement for 1000 nm high sidewalls is 1.5 to 3 time higher than for 300 nm sidewalls due to increased confinement by the sidewall mirrors. Our 3D simulations generally did not produce transmission peaks in the near-infrared.

these structures, it is possible to arrange them in a configuration similar to a 96-well plate. In conjunction with a nano- or microfluidic delivery system, each cup could be capable of functioning as an independent bioreactor. Additionally, because of their independent sensing capabilities, cups can be arranged in linear arrays and used to monitor solution mixing in fluidic channels.

With these various applications in mind, we performed refractive index sensing experiments using our devices. Results of refractive index sensing with two liquids (distilled water n=1.33 and glycerin n=1.351) show an initial bulk sensitivity as high as 390 nm/RIU, which is comparable to other similar devices made by our group and others. Refractive index sensing spectra can be seen in Figure 24a. These spectra were collected by imaging a 900 nm radius cup using backside illumination. A glass coverslip was used to contain solvents on the device. Collected spectra were normalized in order to directly compare peak shifts. These peak shifts can be attributed to changing cup-side plasmon resonances. These sensitivities, while not outstanding in and of themselves, are usable for biosensing applications. The uniqueness of this device does not necessarily derive from it's high

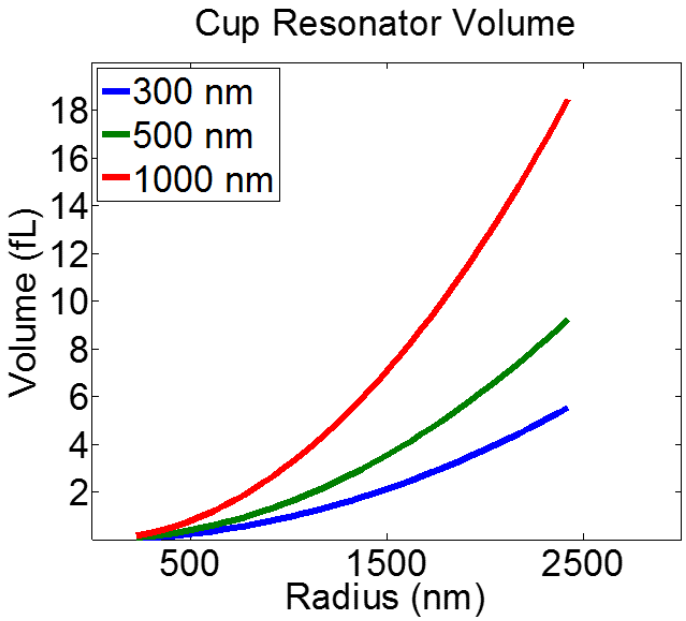

Figure 23: Cup volumes plotted for sidewall heights of 300, 500 and 1000 nm.

sensitivity, but from it's unique structure, which could be useful for many biosensing applications.

By using HSQ patterned devices, it is possible to physically trap surface molecules in the sensor. To test this, we deposited single lipid bilayers on our device substrates, with the hope of collecting free-floating lipid raft domains in the microwell structures. Lipid rafts are glycolipoprotien microdomains in a lipid membrane. In cells, they help facilitate the organization of signaling molecules in the membrane. In physical terms, they are referred to as liquid-ordered (L_o) domains (lipid raft), against the background of a liquid disordered (L_d) domain (lipid bilayer). L_o domains are intrinsically several nanometers thicker, more rigid, and have higher spontaneous curvature than L_d domains, and because of this, they are able to 'float' freely throughout the L_d domains, often localized in areas of highly curved membrane surface because of the favorable energy conditions in these areas [40].

Initially we chose to use unmilled structures to reduce complexity and conserve resources (in case the growth experiments failed). Figure 25 shows these results. We first coated our substrates with a layer of silicon dioxide ($\sim$ 20 nm thick) to promote the deposition of lipids in bilayer structures. This was achieved by depositing a solution containing lipid vesicles was deposited on top of the sample. The vesicles were specially prepared to cover the cup-patterned array, spontaneously (naturally rupturing without exter-

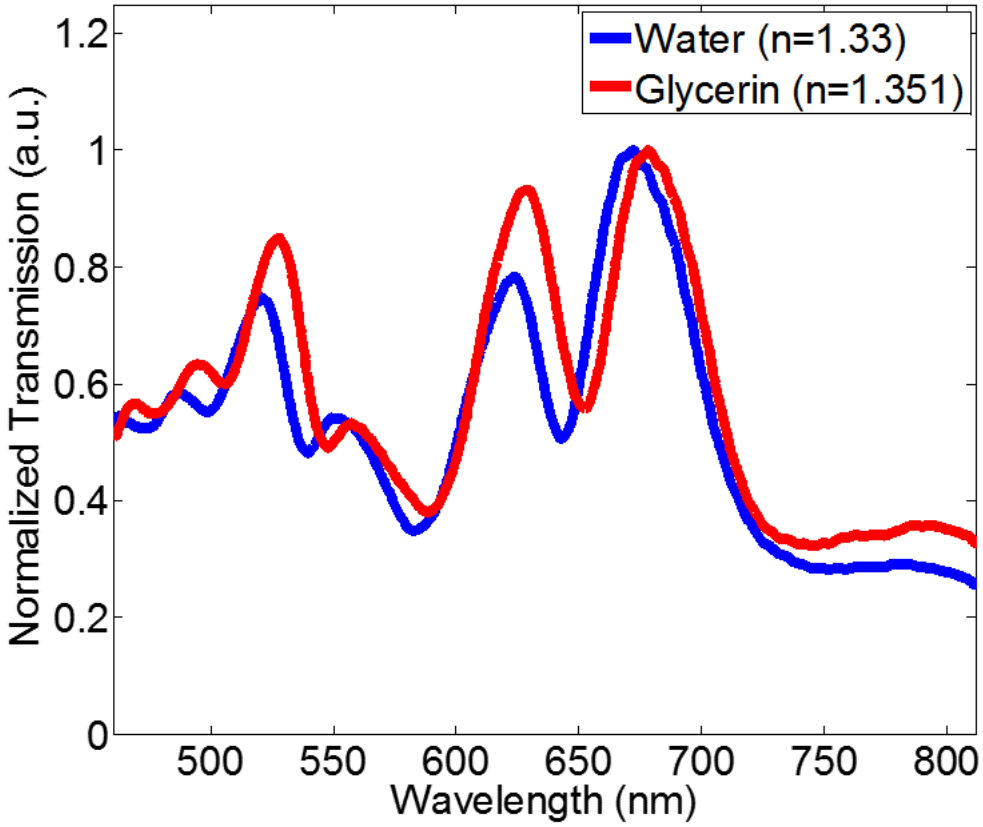

Figure 24: Refractive index sensing data from a 900 nm radius cup. Data was collected using backside illumination. Shifts are caused by changes in cup-side plasmon resonances.

nal force) forming a single lipid bilayer on the silicon dioxide layer. Then, over a period of 150 hours, lipid rafts coalesced inside the cup structures, inwardly, from the outermost edge of the cup. This proved the feasibility of using these structures to collect active surface molecules and demonstrates the potential for further use in biological sensing applications. Based on the sensitivity of our structures we believe we should be able to sense a change in surface refractive index caused by the formation of lipid rafts. Due to time constraints, this has not yet been attempted with fully functioning cup resonators.

4 Conclusion

In conclusion, we have successfully demonstrated the fabrication, characterization, and application of novel cup resonator plasmonic biosensors. Utilizing plasmonic confinement to enhance and modulate transmission

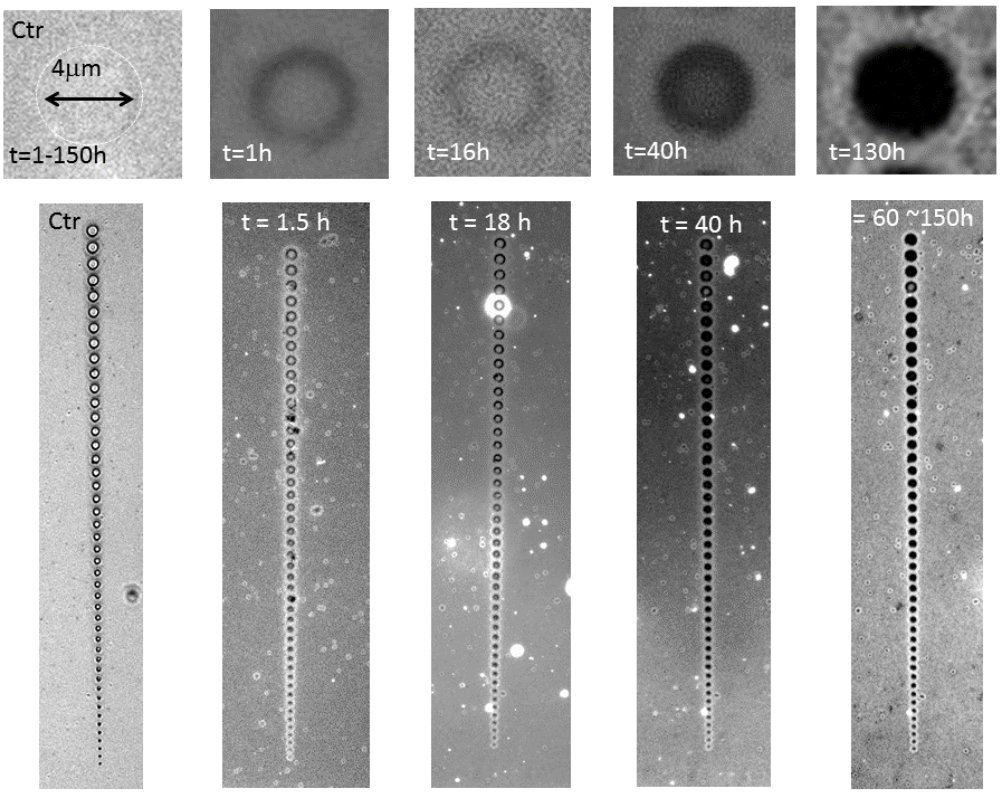

Figure 25: Collection of lipid rafts in the cup resonator structures. The top row shows the gradual amalgamation of lipid rafts over a period of 130 hours in one cup. The bottom row shows the collection of lipid rafts over 150 hours in the entire array. (Data collected by Yong-Sang Ryu. Used with permission.)

through a subwavelength nanohole aperture, the resulting transmission spectra can be used to probe material properties of the dielectric materials inside the sensing volume. We have determined, through measured and simulated data, the physical mechanisms causing transmission modulation in the structure, and using this information, we have constructed predictive behavior models which can be used to design future iterations of these devices for specific purposes. We have shown that these structures are responsive to refractive index changes in their surroundings, and have shown that there are possible application of these structures in biological sensing roles. We have incorporated the unique physical structure of these devices to act as a physical trap for free-floating lipid raft domains, demonstrating the need and usefulness of these devices in the biosensing community.

References

[1] S. A. Maier, *Plasmonics: Fundamentals and Applications*. Springer, 2007.

[2] D. J. Griffiths, *Introduction to Electrodynamics*. 3rd ed., 1999.

[3] N. C. Lindquist, *Engineering metallic nanostructures for surface plasmon resonance sensing*. Dissertation, University of Minnesota, 2010.

[4] A. Zangwill, *Modern Electrodynamics*. 2013.

[5] D. Speiser and K. Williams, *Discovering the Principles of Mechanics 1600-1800: Essays*. Basel: Birkhauser, 2008.

[6] J. C. Maxwell, *The Scientific Papers of James Clerk Maxwell, Vol. I*. Dover Publications, 2013.

[7] B. Hüttner, "A new method for the determination of the optical mass of electrons in metals," *Journal of Physics: Condensed Matter*, vol. 8, no. 50, pp. 11041–11052, 1999.

[8] K.-i. Murata and H. Tanaka, "Surface-wetting effects on the liquid-liquid transition of a single-component molecular liquid.," *Nature communications*, vol. 1, p. 16, 2010.

[9] A. Yariv and P. Yeh, *Photonics: Optical Electronics in Modern Communications*. Oxford University Press, 6th ed., 2007.

[10] P. B. Johnson and R. W. Christy, "Optical constants of the noble metals," *Physical Review B*, vol. 6, no. 12, pp. 4370–4379, 1972.

[11] R. Slavík, J. Homola, and H. Vaisocherová, "Advanced biosensing using simultaneous excitation of short and long range surface plasmons," 2006.

[12] B. Zeng, Y. Gao, and F. J. Bartoli, "Differentiating surface and bulk interactions in nanoplasmonic interferometric sensor arrays.," *Nanoscale*, vol. 7, pp. 166–70, Jan. 2015.

[13] L. Martín-Moreno, F. J. García-Vidal, H. J. Lezec, A. Degiron, and T. W. Ebbesen, "Theory of highly directional emission from a single subwavelength aperture surrounded by surface corrugations.," *Physical review letters*, vol. 90, no. 16, p. 167401, 2003.

[14] F. López-Tejeira, S. G. Rodrigo, L. Martín-Moreno, F. J. García-Vidal, E. Devaux, T. W. Ebbesen, J. R. Krenn, I. P. Radko, S. I. Bozhevolnyi, M. U. González, J. C. Weeber, and a. Dereux, "Efficient unidirectional nanoslit couplers for surface plasmons," *Nature Physics*, vol. 3, pp. 324–328, Apr. 2007.

[15] V. V. Temnov, U. Woggon, J. Dintinger, E. Devaux, and T. W. Ebbesen, "Surface plasmon interferometry: measuring group velocity of surface plasmons.," *Optics letters*, vol. 32, no. 10, pp. 1235–1237, 2007.

[16] J. Feng, V. S. Siu, A. Roelke, V. Mehta, S. Y. Rhieu, G. T. R. Palmore, and D. Pacifici, "Nanoscale plasmonic interferometers for multispectral, high-throughput biochemical sensing.," *Nano letters*, vol. 12, pp. 602–9, Feb. 2012.

[17] L. Chen, J. T. Robinson, and M. Lipson, "Role of radiation and surface plasmon polaritons in the optical interactions between a nano-slit and a nano-groove on a metal surface," *Optics Express*, vol. 14, no. 26, p. 12629, 2006.

[18] Y. Gao, Q. Gan, Z. Xin, X. Cheng, and F. J. Bartoli, "Plasmonic Mach-Zehnder interferometer for ultrasensitive on-chip biosensing.," *ACS Nano*, vol. 5, pp. 9836–44, Dec. 2011.

[19] Y. Gao, Z. Xin, Q. Gan, X. Cheng, and F. J. Bartoli, "Plasmonic interferometers for label-free multiplexed sensing.," *Optics Express*, vol. 21, pp. 5859–71, Mar. 2013.

[20] J. Chen, Z. Li, S. Yue, and Q. Gong, "Efficient unidirectional generation of surface plasmon polaritons with asymmetric single-nanoslit," *Applied Physics Letters*, vol. 97, no. 4, pp. 1–4, 2010.

[21] J. Chen, Z. Li, M. Lei, S. Yue, J. Xiao, and Q. Gong, "Broadband unidirectional generation of surface plasmon polaritons with dielectric-film-coated asymmetric single-slit.," *Optics express*, vol. 19, pp. 26463–9, Dec. 2011.

[22] J. Chen, Z. Li, S. Yue, J. Xiao, and Q. Gong, "Plasmon-induced transparency in asymmetric T-shape single slit.," *Nano letters*, vol. 12, pp. 2494–8, May 2012.

[23] J. Chen, Z. Li, J. Xiao, and Q. Gong, "Efficient All-Optical Molecule-Plasmon Modulation Based on T-shape Single Slit," *Plasmonics*, vol. 8, no. 2, pp. 233–237, 2013.

[24] Y. Gao, Z. Xin, B. Zeng, Q. Gan, X. Cheng, and F. J. Bartoli, "Plasmonic interferometric sensor arrays for high-performance label-free biomolecular detection.," *Lab on a chip*, vol. 13, pp. 4755–64, Dec. 2013.

[25] F. Ye, M. J. Burns, and M. J. Naughton, "Plasmonic halos–optical surface plasmon drumhead modes.," *Nano letters*, vol. 13, pp. 519–23, Feb. 2013.

[26] X. Zhu, J. Zhang, J. Xu, H. Li, X. Wu, Z. Liao, Q. Zhao, and D. Yu, "Dispersion control in plasmonic open nanocavities," *ACS Nano*, vol. 5, no. 8, pp. 6546–6552, 2011.

[27] X. Zhu, Y. Zhang, J. Zhang, J. Xu, Y. Ma, Z. Li, and D. Yu, "Ultrafine and smooth full metal nanostructures for plasmonics.," *Advanced materials (Deerfield Beach, Fla.)*, vol. 22, pp. 4345–9, Oct. 2010.

[28] X. Zhu, J. Zhang, J. Xu, and D. Yu, "Vertical plasmonic resonant nanocavities.," *Nano letters*, vol. 11, pp. 1117–21, Mar. 2011.

[29] P. Nagpal, N. C. Lindquist, S.-H. Oh, and D. J. Norris, "Ultrasmooth patterned metals for plasmonics and metamaterials.," *Science (New York, N.Y.)*, vol. 325, no. 5940, pp. 594–597, 2009.

[30] H.-C. Liou and J. Pretzer, "Effect of curing temperature on the mechanical properties of hydrogen silsesquioxane thin films," *Thin Solid Films*, vol. 335, no. 1-2, pp. 186–191, 1998.

[31] I. Horcas, R. Fernández, J. M. Gómez-Rodríguez, J. Colchero, J. Gómez-Herrero, and A. M. Baro, "WSXM: A software for scanning probe microscopy and a tool for nanotechnology," *Review of Scientific Instruments*, vol. 78, no. 1, 2007.

[32] J. Hyuk Park, P. Nagpal, S.-H. Oh, and D. J. Norris, "Improved dielectric functions in metallic films obtained via template stripping," *Applied Physics Letters*, vol. 100, no. 8, p. 081105, 2012.

[33] K. M. Mcpeak, S. V. Jayanti, S. J. P. Kress, S. Meyer, S. Iotti, A. Rossinelli, and D. J. Norris, "Plasmonic Films Can Easily Be Better: Rules and Recipes," *ACS Photonics*, 2015.

[34] R. Gordon, L. K. K. Swaroop, D. Lepage, and A. G. Brolo, "Resonant light transmission through a nanohole in a metal film," in *2005 5th IEEE Conference on Nanotechnology*, vol. 1, pp. 559–562, 2005.

[35] J. A. Thornton, "The microstructure of sputter-deposited coatings," 1986.

[36] Q. Min and R. Gordon, "Surface plasmon microcavity for resonant transmission through a slit in a gold film.," *Optics express*, vol. 16, no. 13, pp. 9708–9713, 2008.

[37] V. J. Sorger, R. F. Oulton, J. Yao, and G. Bartal, "Plasmonic Fabry-Perot Nanocavity," *Nano letters*, 2009.

[38] W. Yao, S. Liu, H. Liao, Z. Li, C. Sun, J. Chen, and Q. Gong, "Efficient Directional Excitation of Surface Plasmons by a Single-Element Nanoantenna," *Nano Letters*, p. 150407103454003, 2015.

[39] N. C. Lindquist, A. Lesuffleur, and S. H. Oh, "Lateral confinement of surface plasmons and polarization-dependent optical transmission using nanohole arrays with a surrounding rectangular Bragg resonator," *Applied Physics Letters*, vol. 91, no. 25, 2007.

[40] Y.-S. Ryu, I.-H. Lee, J.-H. Suh, S. C. Park, S. Oh, L. R. Jordan, N. J. Wittenberg, S.-H. Oh, N. L. Jeon, B. Lee, A. N. Parikh, and S.-D. Lee, "Reconstituting ring-rafts in bud-mimicking topography of model membranes.," *Nature communications*, vol. 5, p. 4507, 2014.